

Characterization of the western Pictor A hotspot in the hard X-rays with *NuSTAR*

AAMIL SHAIK,¹ EILEEN T. MEYER,¹ KARTHIK REDDY,¹ SIBASISH LAHA,^{2,3,4} AND MARKOS GEORGANOPOULOS¹

¹*Department of Physics
University of Maryland Baltimore County
1000 Hilltop Circle Baltimore
MD 21250, USA*

²*Center for Space Science and Technology, University of Maryland Baltimore County, 1000 Hilltop Circle, Baltimore, MD 21250, USA.*

³*Astrophysics Science Division, NASA Goddard Space Flight Center, Greenbelt, MD 20771, USA.*

⁴*Center for Research and Exploration in Space Science and Technology, NASA/GSFC, Greenbelt, Maryland 20771, USA*

(Received August 8, 2023; Revised May 6, 2024; Accepted May 21, 2024)

ABSTRACT

The origin of X-ray emission from the resolved kiloparsec-scale jets and hotspots of many active galactic nuclei (AGN) remains uncertain, particularly where the X-ray emission is separate from the radio-optical synchrotron component. Possible explanations include synchrotron emission from a second electron population and external Compton or synchrotron self-Compton processes – alternatives which imply very different physical conditions within the jet. Until recently, X-ray studies of resolved jets and hotspots have been restricted to below ~ 10 keV, often showing a hard spectral index indicating a spectral peak beyond this energy range. Here we present *NuSTAR* observations of the nearby powerful radio galaxy Pictor A, in which we clearly detect the western hotspot at approximately 4' from the host galaxy, the most significant detection of hotspot emission above 10 keV to date. The *NuSTAR* spectrum is best fit by a single powerlaw of index $\Gamma = 2.03 \pm 0.04$; an exponential cut-off gives a 1σ lower limit on the cutoff energy of 40.7 keV. We confirm previous findings of variations in the soft X-ray flux detected by *Chandra* over the 2000 to 2015 period, at a significance of 6.5σ . This rises to $> 8\sigma$ in the common 3-8 keV band using the combined 22-year span of *Chandra* and *NuSTAR* observations. The variability of the western Pictor A hotspot strongly confirms the previously argued synchrotron nature of the X-ray emission for the hotspot, while the lower bound to the spectral cutoff energy implies electron energies in the hotspot reach up to at least a few TeV.

Keywords: X-rays: galaxies – galaxies: active – galaxies: jets – quasars: individual (Pictor A)

1. INTRODUCTION

A fraction of active galactic nuclei (AGN) launch large, collimated jets of relativistic plasma (Blandford & Königl 1979). These jets can transport energy and matter up to Megaparsec distances from the central black hole in the most extreme cases (Dabhade et al. 2020). In more powerful jets, the relativistic jet can extend into the intergalactic medium (IGM), creating a bright, terminal hotspot where the kinetic energy of the jet is injected into large, extended lobes of cooling plasma. The power and extent of AGN jets is such that they can produce Mpc-scale shocks and cavities in the IGM and the intercluster medium and are thought to have a significant impact on the star-formation rate of the host galaxy (McNamara et al. 2009; Fabian 2012).

AGN jets and hotspots are both primarily detected at radio and sometimes IR/optical frequencies where they emit synchrotron radiation from electrons gyrating within the jet magnetic field (e.g., Meisenheimer et al. 1997; Werner et al. 2012). For this reason, jetted AGN are more ‘radio-loud’ compared to the majority of non-jetted AGN. Sources where the jet is aligned in the plane of the sky are known as radio galaxies. Radio galaxies are often divided into two classifications based on jet morphology: Fanaroff & Riley type I (FR I; Fanaroff & Riley 1974) jets tend to be shorter, less collimated, and brightest near the central engine with the jet typically terminating in large, darkened plumes of plasma, while FR II jets are highly collimated and brightest and exhibit terminal hotspots.

Low-spatial-resolution photometric observations of jetted AGN are usually dominated by emission from the highly relativistic base of the jet (sometimes called the ‘core’ due to appearance in e.g., radio-band imaging). The focus of this study is on the emission of the extended jet, from $\sim 0.1 - 100$ kpc from the central engine. At these scales, the kpc-scale jet extends into and beyond the host galaxy and can be resolved in high-resolution imaging with e.g. the Hubble Space Telescope, the Very Large Array, and the *Chandra* X-ray Observatory.

One of the major discoveries of *Chandra* was the detection of bright X-ray emission from resolved radio jets and hotspots on kpc scales (Chartas et al. 2000; Sambruna et al. 2001). In some FRI jets lacking hotspots such as M87 (Harris et al. 2003; Sun et al. 2018) and Cen A (Kraft et al. 2002; Snios et al. 2019), the X-ray emission is roughly consistent with a single spectral component extending from radio to optical to X-rays. In other, often more powerful jets (Harris & Krawczynski 2006, 2007; Harris et al. 2010; Marshall et al. 2010) the X-ray emission is often ‘anomalous’, meaning that the X-ray flux from the jet and terminal hotspot is too bright and hard-spectrum to be an extension of the primary radio-optical synchrotron component.

For kpc-scale anomalous jets (here we use ‘jet’ to mean the resolved components extending up to but not including the hotspot), the initially preferred explanation of inverse Compton scattering of the CMB (IC-CMB) has largely been overturned in favor of a synchrotron origin for the X-rays, at least in jets a lower redshift (e.g. Tavecchio et al. 2000; Celotti et al. 2001; Sambruna et al. 2004; Jester et al. 2006; Meyer et al. 2016; Breiding et al. 2017, 2023; Meyer et al. 2023).

In hotspots the case is somewhat different; thought to represent the jet terminus where the flow finally decelerates to sub-relativistic bulk speed, the IC-CMB contributions are expected to be negligible. While many hotspots are adequately explained as synchrotron self-Compton (SSC) emission (Harris et al. 1994; Hardcastle et al. 2002; Arshakian & Longair 2000), others are not, requiring magnetic fields grossly out of equipartition (Hardcastle et al. 2004). An SSC origin is also incompatible with the sometimes observed large spatial offsets between the radio and X-rays (Erlund et al. 2007; Reddy et al. 2023). Beaming models based on jet electrons upstream of the termination shock where the flow is still relativistic scattering post-shock radio emission have been proposed (Georganopoulos & Kazanas 2003; Worrall et al. 2012), but there is limited evidence to support the conclusion that beaming strongly impacts hotspot X-ray emission across the jet population (e.g. Mullin et al. 2008; Hardcastle et al. 2016) and more recent work suggests that the X-ray emission in many hotspots is due synchrotron emission from a second population of electrons, as has been found for many jets (e.g. Mingo et al. 2017).

The source of the kpc-scale X-ray emission for powerful jets and hotspots is a longstanding open question. In some cases alternate models imply orders-of-magnitude differences in jet kinetic power and magnetic field strength. Determining to what extent each possible mechanism contributes across the X-ray jet and hotspot population is thus important also for understanding the energy content of jets and their impact. Given the unsolved origin of the X-ray emission, it is useful to attempt to extend the spectral coverage with observations in the hard X-ray range ($E > 10$ keV). If the emission is synchrotron in origin, locating the turnover point where the spectrum begins to fall can place constraints on the maximum electron energy. This energy range is covered by *NuSTAR*, but observations of kpc-scale jets are complicated by the fact that *NuSTAR* lacks the angular resolution (FWHM $\sim 7.5''$) to easily distinguish the kpc-scale jet from the core in most sources. Given these limitations, the outer jet and western hotspot of FR II radio galaxy Pictor A ($z = 0.035$; 0.69 kpc $''$) is nearly the only jet with the sufficient angular separation ($\sim 4'$) from the core to be a viable target for hard X-ray study and the only one bright enough to be detected by *NuSTAR* in less than approximately 1 Ms of exposure.

Pictor A is among the most well-studied X-ray jets in the literature, and, along with its hotspot, has been the subject of a number of detailed studies over the past two decades (e.g., Wilson et al. 2001; Hardcastle et al. 2004; Hardcastle & Croston 2005; Migliori et al. 2007; Tingay et al. 2008; Marshall et al. 2010; Hardcastle et al. 2016; Thimmappa et al. 2020). The X-ray jet was first reported by Wilson et al. (2001) and was noted to be X-ray-anomalous by Hardcastle et al. (2004). Despite its bright X-ray emission, it is not a source which we would expect a significant IC-CMB component as it has a low redshift, its (approaching) western jet is not closely inclined to our line-of-sight ($\theta \sim 20 - 45^\circ$), and its counterjet is clearly visible (Hardcastle & Croston 2005). A beamed inverse-Compton origin for the X-rays from the jet or hotspot would require magnetic field strengths significantly below equipartition values (Hardcastle et al. 2004). The deepest observation of the jet and hotspot to date in the soft X-rays combined 464 ks of *Chandra* exposure on the western hotspot, finding a spectrum near-equally consistent with a single constant powerlaw spectrum with $\Gamma = 1.94 \pm 0.01$ or a steepening, broken powerlaw spectrum with $\Gamma_1 = 1.86 \pm 0.02$, $\Gamma_2 = 2.16 \pm 0.05$, and a break energy at around 2 keV (Hardcastle et al. 2016). One of the motivations for our deep *NuSTAR* observation was

to clarify the presence and location of a possible spectral break or cutoff in the broad X-ray band. Previous research of the hard X-ray emission from the hotspot found no evidence of such a spectral break or cutoff (Sunada et al. 2022); however, as discussed below, the addition of new *NuSTAR* observations affords us the opportunity to reexamine the spectrum with greater significance.

The jet of Pic A is also noteworthy for the detection of variability in the X-rays. In 2010, Marshall et al. (2010) analyzed three *Chandra* observations taken in 2000, 2002, and 2009 of 26, 96, and 54 ks of exposure time respectively. They found that the soft X-ray flux of two features located at 34 and 49 kpc away from the core decreased significantly (3.4σ and $\sim 3\sigma$ respectively) over the course of the observations. The later Hardcastle et al. (2016) study (with an additional 6 *Chandra* observations) found the hotspot X-ray flux decreased by $\sim 10\%$ over a time period of approximately one month, and confirmed $\sim 3\sigma$ variability in the jet. Recently, Pictor A was included in a large archival study of *Chandra* jet observations where at least five regions in the jet, including the hotspot, were found to be variable (Meyer et al. 2023); we further expand on the results of that study here using the same methods. The IC-CMB mechanism requires low-energy electrons ($\gamma \sim 100 - 1000$) with cooling timescales on the order of $\sim 10^5 - 10^6$ yrs (Worrall 2009), so the observed variability in the X-ray flux is clearly incompatible with such an origin. Furthermore, the fast timescales of the variability allow us to probe the physical conditions within the hotspot, most notably the size of the emitting regions (Tingay et al. 2008).

In this paper, we report the results of a comprehensive X-ray spectral analysis of the western hotspot of Pictor A, including new and archival *NuSTAR* observations totalling 348 ks. We combine this with 313 ks of archival *Chandra* data from 11 different observations with the Advanced CCD Imaging Spectrometer (ACIS; Garmire et al. 2003) and modeled the combined wide X-ray band spectrum (0.5 – 20 keV). A similar research project was undertaken by Sunada et al. (2022); however, access to an additional 300 ks of *NuSTAR* data allows us to place stricter constraints on the hard and broadband X-ray spectrum than previously possible. We also used the maximum likelihood method of Meyer et al. (2023) to test for variability in the *NuSTAR* and *Chandra* observations, and discuss the implications of our findings for the X-ray emission origin in Pictor A.

2. OBSERVATIONS AND DATA REDUCTION

2.1. NuSTAR observations

The *NuSTAR* observatory consists of two independent, co-aligned X-ray telescopes, and was launched into orbit in 2012 (Harrison et al. 2013; Madsen et al. 2014). The telescopes each have an array of grazing incidence X-ray mirrors arranged in a conical approximation of a Wolter I geometry, which are designated as Optical Module A (OMA) and Optical Module B (OMB). OMA and OMB focus incoming X-rays within the $13' \times 13'$ FOV onto two modules of solid state detector arrays, which are designated as Focal Plane Module A (FPMA) and Focal Plane Module B (FPMB).

NuSTAR first observed the western hotspot of Pictor A in 2015 with an exposure of 109 ks. A second observation was proposed and completed in 2021, consisting of 3 pointings totaling 302 ks of exposure. We group these later observations into a single ‘epoch’, or collection of observations conducted within a short timeframe of one another ($t_{sep} \leq 1$ wk). The details of the 2 *NuSTAR* epochs and their constituent observations which are used in this study are included in Table 1, which lists the project code, observation date, PI, the epoch grouping, and the exposure time before and after filtering.

We downloaded the raw *NuSTAR* data from *HEASARC* and applied the standardized procedure to reduce and image the data using the `nupipeline` command from the *NuSTAR* Data Analysis Software (*NuSTARDAS*) v2.1.0¹, which is included in the *HEASARC* software package (*HEASOFT*) v6.29². In particular, we excised time intervals where background radiation and contamination from the South Atlantic Anomaly (SAA) was significant using the `nupipeline` settings `SAA = STRICT` and `TENTACLE = YES`. At this stage, we filtered the data to the energy range of 3-78 keV.

Once the data were filtered, we created a circular extraction region of radius $50''$ at the centroid of the hotspot. We used the `nuproducts` pipeline to generate high-level data products for the source region, including extracted photon counts spectral files (PHAs), auxiliary response files (ARFs), response matrix files (RMFs), and exposure maps. This process was repeated for both the FPMA and FPMB images from each *NuSTAR* observation, giving us 8 total sets of *NuSTAR* data.

¹ https://heasarc.gsfc.nasa.gov/docs/nustar/analysis/nustar_swguide.pdf

² https://heasarc.gsfc.nasa.gov/docs/software/heasoft/developers_guide/

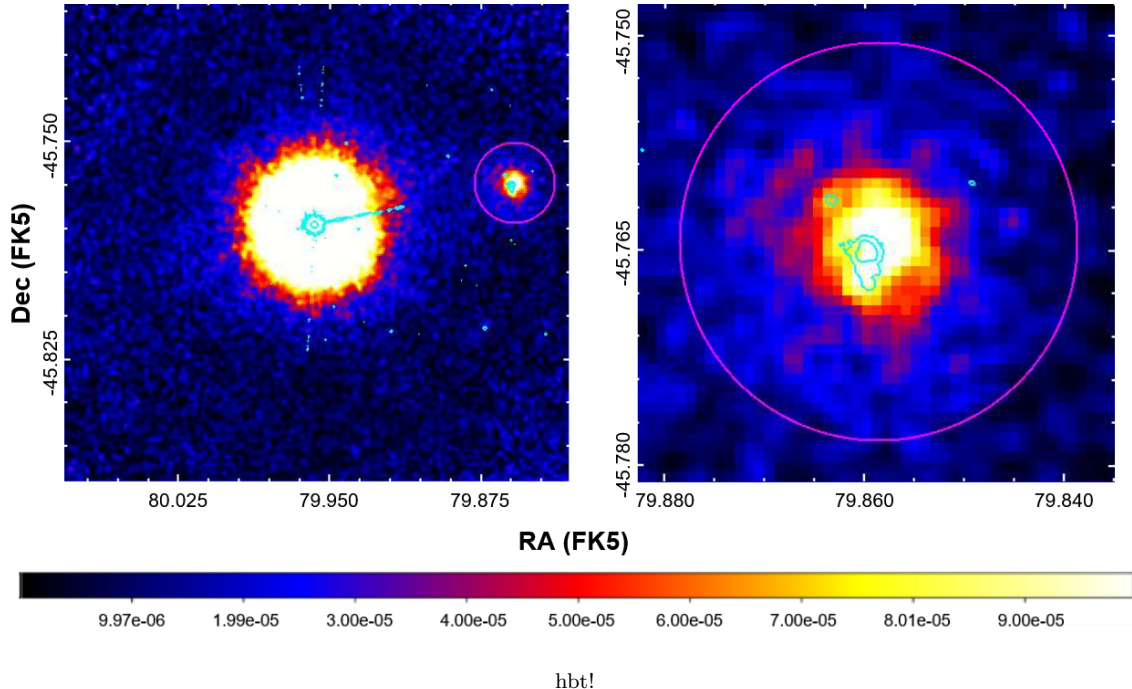


Figure 1. (Left) The final combined *NuSTAR* image of Pictor A using FPMA and FPMB data from epochs 1 and 2. The images from each observation are aligned using cross-correlations of the bright core. The images are then background-subtracted and exposure-corrected using background- and exposure-maps generated by `nuskybgd` and `nuproducts`, respectively. The individual flux images are then averaged, and smoothed by a Gaussian at a factor of 2 pixels ($4.8''$) to produce the image above. The $50''$ extraction region used for spectral analysis is encircled in magenta. The overlaid contours are taken from combined *Chandra* data. (Right) An expanded image of the source region and western hotspot, again with *Chandra* contours overlaid. Unlike the high-resolution imaging of *Chandra*, *NuSTAR* is unable to resolve any structures or morphological features within the hotspot. The colorbar below shows the image flux scale in units of $\text{ph s}^{-1} \text{cm}^{-2}$.

For visual study of the jet and environs, we created a hard X-ray image using the combined data of all available *NuSTAR* observations. We used the `nuskybgd` code developed by Wik et al. (2014) to generate background-subtracted images (see Section 2.3 for more details). We used the background-subtracted images and the CIAO commands `dmstat` and `acrosscorr` to calculate the centroid position of the auto-correlated image of the earliest FPMA observation of the X-ray core, calculating the offsets in the centroid positions of later observations, and reprojecting the later observations such that the X-ray core is aligned. We used the same offsets to align the exposure maps generated by `nuproducts`. We co-added all our aligned *NuSTAR* observations and divided the resulting deep photon image by the similarly co-added exposure map to obtain a hard X-ray flux image of Pictor A. Lastly, we applied a Gaussian smoothing filter on the image at a factor of 2 pixels ($4.8''$) to produce our final image, which is shown in Figure 1, with *Chandra* contours overlaid.

The peak of the hotspot emission profile as seen by *NuSTAR* at first appears slightly offset from the peak observed by *Chandra*, by approximately $4\text{--}5''$ downstream along the jet axis. If real, this offset would place the hard X-ray centroid beyond even the radio peak, which is estimated to be downstream of the *Chandra* position by approximately $1''$ (Hardcastle et al. 2016). However, there are two factors which lead us to doubt the reality of the offset: first, there is substantial uncertainty in the centroid position, with $dx, dy = 1.72'', 2.42''$ respectively, where we use the root mean square correction obtained from cross-correlations on the *NuSTAR* images with the `acrosscorr` command. In addition, asymmetries in the effective PSF may bias the apparent position of the hotspot – indeed deconvolved *NuSTAR* images do not show an offset (see further discussion and images in section 2.7).

2.2. Chandra observations

The *Chandra* X-ray Observatory was launched in 1999 as a part of NASA’s Great Observatories program (Weisskopf et al. 2000). The ACIS-S CCD detector (Garmire et al. 2003) onboard has an unrivaled subarcsecond angular resolution

Table 1. *NuSTAR* and *Chandra* observations of Pictor A

Instrument	Epoch	Project Code	Date Obs. (YYYY-MM-DD)	Exposure (ks)	Filtered Exposure (ks)	PI
<i>NuSTAR</i>	1	60101047002	2015-12-03	109.5	92.82	Croston
	2	60701064002	2021-11-28	126.2	104.1	Meyer
	2	60701064004	2021-12-01	37.59	32.39	Meyer
	2	60701064006	2021-12-02	138.8	118.6	Meyer
	Total	-	-	412.1	347.9	-
<i>Chandra</i>	1	346	2000-01-18	25.83	25.07	Wilson
	2	3090	2002-09-17	46.36	31.23	Wilson
	2	4369	2002-09-22	49.12	34.53	Wilson
	3	11586	2009-12-12	14.26	12.21	Hardcastle
	3	12039	2009-12-07	23.74	21.95	Hardcastle
	3	12040	2009-12-09	17.32	15.62	Hardcastle
	4	14221	2012-11-06	37.48	35.18	Hardcastle
	4	15580	2012-11-08	10.48	9.97	Hardcastle
	5	14222	2014-01-17	45.38	44.03	Hardcastle
	6	14223	2014-04-21	50.14	42.20	Hardcastle
	7	16478	2015-01-09	26.82	23.75	Hardcastle
	7	17574	2015-01-10	18.62	17.34	Hardcastle
	Total	-	-	365.6	313.1	-

in the 0.3 - 10.0 keV energy range, making it ideal for observing kiloparsec-scale extragalactic X-ray jets. *Chandra* has observed Pictor A in 16 separate pointings, from the initial discovery of the large-scale X-ray jet in 2000 (Wilson et al. 2001) to subsequent observations of the jet and hotspot as recently as 2015 (Hardcastle et al. 2004; Hardcastle & Croston 2005; Hardcastle et al. 2016). A few observations were excluded from this analysis due to extremely short exposure. Similar to our *NuSTAR* observations, we grouped observations conducted within ~ 1 week of one another into single epochs. Ultimately, we made use of use 11 *Chandra* observations which are grouped into 7 epochs and totaling a nominal 360 ks of exposure time. A full list of the *Chandra* observations used in this analysis, their epoch groupings, PI, project code, observation date, and exposure time before and after filtering can be found in Table 1, alongside the *NuSTAR* epochs and observations described in the previous section.

Two observations included in previous deep surveys of Pictor A (Hardcastle et al. 2016; Sunada et al. 2022) have been excluded from this study. The observation corresponding to project code 14357 has the hotspot positioned on a separate chip from the rest of the observation. To minimize complications of differences between the chips, it has been excluded. Similarly, in the observation corresponding to project code 15593, the hotspot is positioned exactly on the chip edge. This complicates the extraction of spectra from the hotspot, and so this observation was also excluded from our analysis.

All observations were reduced using CIAO version 4.1.2 (Fruscione et al. 2006) and the calibration database CALDB v. 4.9.2. Each observation was first reprocessed using the `chandra_repro` and filtered to remove all photons outside of the 0.4-8 keV range to minimize background contamination. We use the `lc_clean` task to bin the good time interval (GTI) data with a bin time of 259.28 s and excise intervals with background flares, which we define as a photon count rate which deviates from the mean count rate by more than 2σ . We then used this filtered data to produce the 11 sub-pixel images centered on the core of the X-ray jet, one for each epoch, downsizing by a factor of 5 for a pixel scale of $0.0984''$. After filtering, the total exposure time is approximately 313 ks.

We also generated a combined soft X-ray image using all *Chandra* data reduced for this study. We again used cross-correlation to precisely locate the hotspot centroid and structure to correct for astrometric offsets between observations and the exposure maps generated for each observation using the CIAO tool `mkexppmap`. Finally, we combined the aligned images for each *Chandra* epoch using the CIAO tool `dmerge` and divided by the combined exposure map to obtain the final soft X-ray flux image of Pictor A. The final image is presented in Figure 2, with *NuSTAR* contours overlaid.

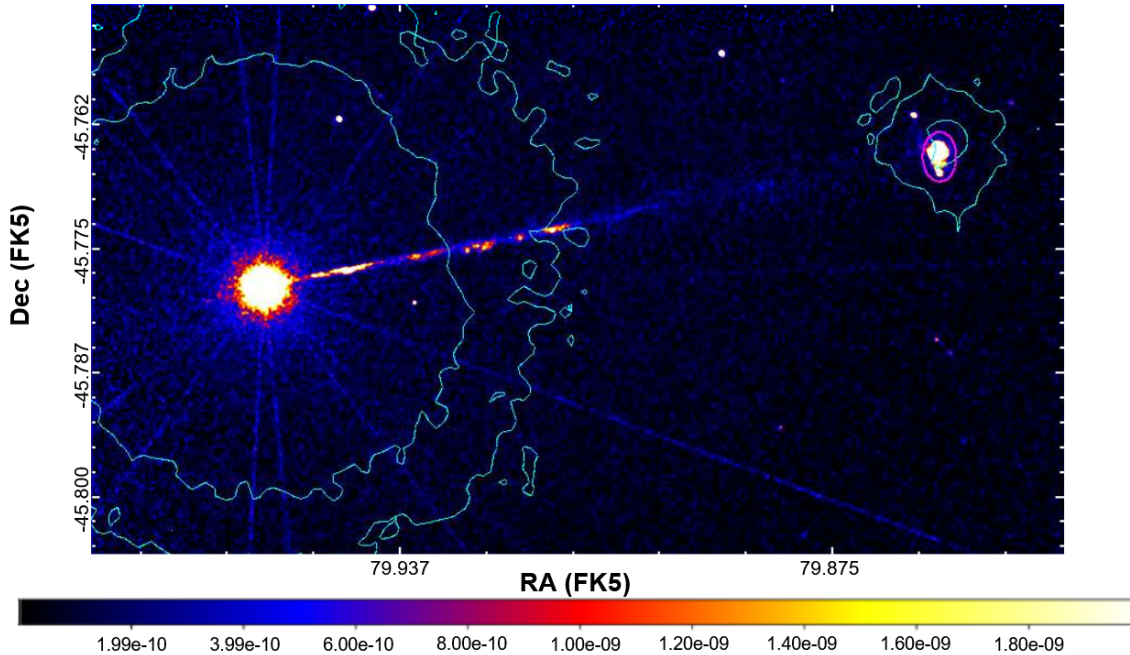


Figure 2. The final combined *Chandra* image of Pictor A using soft X-ray data from all epochs listed in Table 1. The images from each observation are aligned using PSF simulations and cross-correlation of the bright core. The images are then exposure-corrected using exposure-maps generated by the CIAO tool `mkexppmap`. The individual flux images are then averaged together, and the final image is smoothed by a Gaussian at a factor of 8 pixels ($3.92''$). The elliptical extraction region used for spectral analysis is encircled in magenta. The overlaid cyan contours are taken from the combined *NuSTAR* data shown in Figure 1. The colorbar below shows the image flux scale in units of $\text{ph s}^{-1} \text{cm}^{-2}$.

2.3. *NuSTAR* background

The background radiation spectrum for *NuSTAR* observations is complex, including multiple different components which dominate at different energies. Additionally, the background radiation is spatially nonuniform and varies significantly according to the position on the detector.

The background spectra for each module and pointing were modeled and fit using the IDL-based `nuskybgd` code developed by Wik et al. (2014), which maps both the spectral and spatial variations of the background emission across the entire image. The full background model is detailed in Appendix A and the best-fit normalization for each variable parameter for each *NuSTAR* observation is recorded in Supplemental Table 1 in the online version of this article. For all observations, $\chi_{red}^2 = \chi^2/\text{DOF}$ had a value between 0.9 and 1.1, indicating that the background was well fit by the model. Figure 3 shows a visual representation of the complete background model, including the different individual components, taken from Wik et al. (2014) alongside the background spectra observed in one of our *NuSTAR* observations.

We used `nuskybgd` to extract and fit the background spectrum and make a map of the background emission over the detector coordinates for each *NuSTAR* observation. After fitting the background, we provided `nuskybgd` with our source region and created a model file containing the appropriate parameter values for the background spectrum at those detector coordinates.

2.4. *Chandra* background

For each *Chandra* observation, we extracted the background photon counts from a large elliptical region far from the hotspot and bright X-ray core with minor and major axes of $70''$ and $65''$ respectively. The background region position was identical across all *Chandra* epochs and always on the same chip as the hotspot. We used this to generate a background spectral file corresponding to each *Chandra* observation of the hotspot. Whenever fitting *Chandra* data in XSPEC, we use the CSTAT statistic which defaults to WSTAT when background data is loaded but not modeled in

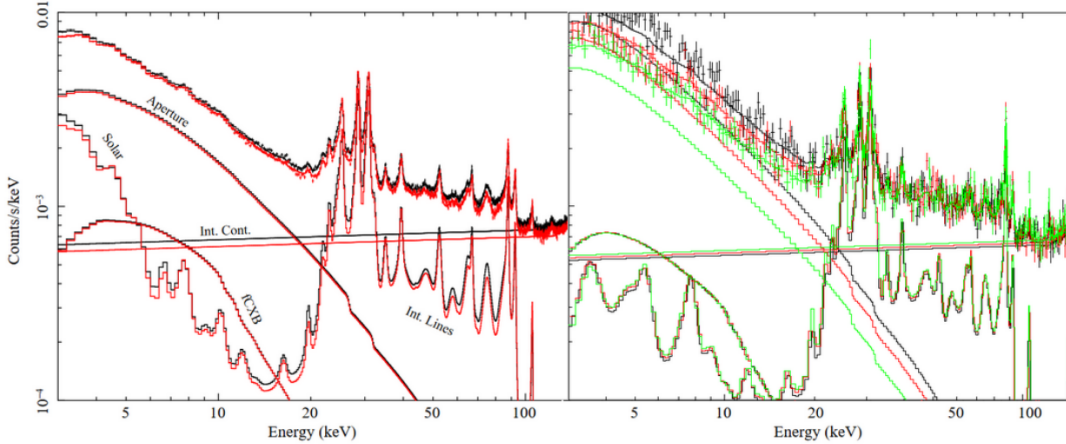


Figure 3. (Left) Image of the various background components and total background spectrum for *NuSTAR*, taken from Wik et al. (2014). The model consists of an aperture background due to stray light leaking into the detector, an internal background consisting of a broken powerlaw and a spectral line continuum, a background of scattered light, and a background due to unresolved X-ray sources in the FOV. (Right) Image of the background fit completed using `nuskybgd`. The code fits background spectra from multiple annular regions which effectively encompass the entirety of the image which contains negligible source emission. The spectra from these different annuli are depicted as the red, green, and black spectra, which are binned to a minimum of 30 counts per bin, fit simultaneously, and used to constrain the spectral parameters and map the spatial variations of the background across the detector.

XSPEC. We bin the spectra such that there are at least 5 counts in the background spectra for each bin to avoid any problematic biases.

2.5. Spectral modeling of the western hotspot

We used XSPEC v12.10.1f and its python interface PyXspec v 2.1.1 for all X-ray spectral analysis. We chose the Poisson-based `cstat` statistic (Cash 1979) for our parameter estimation statistic and the Anderson-Darling (ad) test statistic to evaluate goodness-of-fit. We chose this method to avoid the problematic biases that arise from trying to bin and fit the spectrum using the χ^2 statistic (Andrae et al. 2010). We fit the spectra from *Chandra* and *NuSTAR* separately, then performed a final fit using the combined data set.

For *NuSTAR* observations, we use a $50''$ radius circular region with its center located at the centroid of the western hotspot as our source region. We extracted the source counts from this region for both the FPMA and FPMB image and filtered to an energy range of 3-20 keV. Based on the results of our analysis using `nuskybgd` across the 2 epochs of *NuSTAR* data, we estimate that approximately 3192 counts out of 3542 total counts ($\sim 90\%$) in the energy band of 20-78 keV are the result of background radiation. Therefore, we ignored this higher energy band in our analysis.

When modeling the source spectrum for each *NuSTAR* epoch, we combined FPMA and FPMB data, and introduced a constant factor to our spectral model (`constant` parameter). For the FPMA observations, this constant was fixed to 1, while for FPMB observations, it was free to vary between 0.9 and 1.1. This factor was included to account for the unknown normalization difference between the two detectors which typically varies between $\pm 5\%$ (Madsen et al. 2015). After fitting each *NuSTAR* epoch separately, we performed a total fit using all reduced *NuSTAR* data.

For *Chandra* observations, we extracted the source counts from an elliptical region with minor and major axes of $6''$ and $9''$ respectively and its center located at the centroid of the western hotspot. Just as we did with *NuSTAR*, we fit each *Chandra* epoch separately, and then fit the combined *Chandra* data in an energy range of 0.5-7 keV.

Finally, to maximize our photon statistics and achieve the best constraints on the X-ray spectrum over the wide X-ray band (0.5-20 keV), we fit the combined spectrum of *Chandra* and *NuSTAR* data. We reintroduce the constant factor used to account for offsets between the *NuSTAR* FPMA and FPMB detectors, again freezing it at a value of 1 for the FPMB data and allowing it to vary from 0.9 to 1.1 for FPMA data. We also apply a constant factor to our *Chandra* data to similarly account for the offsets between *NuSTAR* and *Chandra* data (Madsen et al. 2017). We allow this second constant to vary in a range of 0.1-10, given the possibility of intrinsic source variability.

Table 2. Model Definitions and Bayesian Prior Distributions

Model Name	XSPEC Model	Model Formula [$F(E)$]	Parameter Name	Param. No.	Prior Type	Prior Min.	Prior Max.
Powerlaw (PL)*	powerlaw	$NE^{-\Gamma}$	N (N_{1-kev})	2	Log Unif.	-10	0
			PhoIndex (Γ)	1	Unif.	1	3
Broken powerlaw (Bkn. PL)	bknpower	$NE^{-\Gamma_1}, E < E_{brk}$ $NE_{brk}^{\Gamma_2-\Gamma_1} E^{-\Gamma_2}, E > E_{brk}$	N	4	Log Unif.	-10	0
			PhoIndx1 (Γ_1)	1	Unif.	1	3
			BreakE (E_{brk})	2	Unif.	E_{min}	E_{max}
			PhoIndx2 (Γ_2)	3	Unif.	1	3
High-energy cutoff powerlaw	cutoffpl	$NE^{-\Gamma} \exp(-E/\beta)$	N	3	Log Unif.	-10	0
			PhoIndex	1	Unif.	1	3
			HighECutoff	2	Unif.	E_{min}^*	E_{max}
Log-parabola	logpar	$NE^{-\alpha-\beta \log(E)}$	N	4	Log Unif.	-10	0
			alpha	1	Unif.	1	3
			beta	2	Unif.	0	1
Thermal plasma	apec	Smith et al. (2001)	N	16	Log Unif.	-10	0
			kT	1	Unif.	0	30
Double broken powerlaw (Dbl. Bkn. PL)	bkn2power	$NE^{-\Gamma_1}, E < E_{brk,1}$ $NE_{brk,1}^{\Gamma_2-\Gamma_1} E^{-\Gamma_2}, E_{brk,1} < E < E_{brk,2}$ $NE_{brk,1}^{\Gamma_2-\Gamma_1} E_{brk,2}^{\Gamma_3-\Gamma_2} E^{-\Gamma_3}, E > E_{brk,2}$	N	6	Log Unif.	-10	0
			PhoIndx1	1	Unif.	1	3
			BreakE1 ($E_{brk,1}$)	2	Unif.	E_{min}	5
			PhoIndx2 (Γ_2)	3	Unif.	0	4
			BreakE2 ($E_{brk,2}$)	4	Unif.	5	E_{max}
			PhoIndx3 (Γ_3)	5	Unif.	1	3

NOTE— $E_{min} - E_{max}$ is 0.5-8 keV for *Chandra*, 3-20 keV for *NuSTAR*

NOTE— * Abbreviations are provided for the most noteworthy models and their respective parameters which are used to reference them in future tables.

To model the spectrum for a given epoch or epochs, we loaded the corresponding background model or spectral files created through the processes detailed in 2.3 and 2.4. We evaluated the following six spectral models: a powerlaw (**zpowerlw**), a broken powerlaw (**zbknpower**), a double broken powerlaw (**bkn2pow**), a log-parabola (**zlogpar**), a cutoff powerlaw (**zcutoffpl**), and a thermal plasma model (**apec**). For each model, we assumed a redshift of $z = 0.035$ and applied a photoelectric absorption model (**phabs**) with a fixed Hydrogen column density value of $nH = 3.62 \times 10^{-20} \text{ cm}^{-2}$ (HI4PI Collaboration et al. 2016). For the thermal plasma model, we additionally assumed a metallicity of 0.3 times solar values.

We used the Bayesian X-ray Analysis (BXA) software from Buchner (2016), which connects a nested sampling algorithm (UltraNest; Buchner 2021) with the Python version of XSPEC, pyXspec (Gordon & Arnaud 2021). We found this to be the most effective and stable method of spectral fitting. BXA also enables us to easily compare non-nested models using the Bayes' evidence (Z), the likelihood integrated over the parameter space (Knuth et al. 2014). The tested models reflect the possibility of X-ray emission from the hotspot could potentially arise from inverse-Compton scattering, synchrotron radiation, SSC, thermal emission, or any combination of these processes.

We defined our prior distributions such that the analysis spans the entire parameter space. In particular, we defined the priors for our spectral parameters (e.g. Γ) and energy parameters to sample a uniform distribution across all physically reasonable values. The uninformative priors are thought to minimize bias in the posterior distribution. We report the relevant prior distributions for all the free parameters of the evaluated models in Table 2. This table

Table 3. Variability Analysis Data (*NuSTAR*:3-78 keV, *Chandra*: 0.5-8 keV)

Inst.	Proj. Code	Src. Counts (ph)	Bkg. Counts (ph)	Src. Exposure (10^6 cm 2 ·s)	Bkg. Exposure (10^6 cm 2 ·s)	ECF
<i>NuSTAR</i>	60101047002	2127	1304	64.4	-	0.677
	60701064002	3172	1510	109	-	0.671
	60701064004	952	441	34.2	-	0.670
	60701064006	3531	1638	123	-	0.670
<i>Chandra</i>	346	2969	160	11.9	12.1	0.973
	3090	3229	156	12.5	12.3	0.982
	4369	3573	359	13.7	13.5	0.980
	11586	1105	104	3.97	3.89	0.979
	12039	1890	212	7.13	7.00	0.982
	12040	1411	148	5.07	5.06	0.977
	14221	2781	203	9.90	8.63	0.981
	15580	825	54	2.86	2.49	0.978
	14222	3090	256	11.2	11.9	0.980
	14223	2380	194	7.88	8.42	0.981
	16478	1350	148	5.25	5.99	0.984
	17574	1014	115	3.61	4.26	0.976

includes the model name, the XSPEC model name, the model formula, the XSPEC parameter names, the type of prior for the parameter (either uniform or log-uniform), and the minimum and maximum value of the prior distribution.

2.6. Variability analysis

In previous work, Meyer et al. (2023) introduced a maximum-likelihood based statistical test to analyze a series of CCD observations of point sources for variability where the null hypothesis is a non-variable Poisson source rate and a variable background rate. The test uses a maximum likelihood model to return a p-value for a set of single-region observations under the null hypothesis. Previously, this method was used to conduct a variability survey of the large-scale, X-ray jet population using *Chandra* archival data of 53 sources, including Pictor A (Meyer et al. 2023). While *Chandra*'s high angular resolution make it an ideal partner for general tests of unresolved jet variability, the test is generally applicable to e.g. other observatories with CCD detectors. Here we applied the variability test to both our *Chandra* and *NuSTAR* data on Pictor A.

The maximum likelihood test is described in full in Meyer et al. (2023). Here, we will only briefly describe the necessary elements of the test. For each observation entered into our analysis, we required the following data: (1) the total number of photon counts in the source region, (2) the number of background photons in the source region, (3) the exposure in the source region, and (4) the encircled counts fraction (ECF). For the analysis of the *Chandra* alone, we extracted this data for an energy range of 0.4-8 keV, and for *NuSTAR* alone, we extracted it for the full 3-78 keV energy range. We also separately extracted the 3-8 keV counts for a combined analysis using both observatories. We list the values for this data for all observations used in the variability analysis are given in Tables 3 and 4. Using this data, the maximum likelihood model returns an estimate of the source flux, $\bar{\mu}$, under the steady-rate assumption and also the probability of observing the data under the null hypothesis. A low p -value indicates that the null hypothesis can be rejected and that the intrinsic source rate is therefore likely to be variable.

We extracted the number of photon counts in our source region using the CIAO tool `dmextract` and the total exposure for the region using the same method on the exposure maps generated by *NuSTAR*DAS `nuexpomap` for our *NuSTAR* data and CIAO tool `mkexpmap` for our *Chandra* data. To estimate (2) for *Chandra*, we similarly extract the counts and exposures of a corresponding background region and weight the background counts by the ratio of the background exposure to the source exposure. Unlike with *Chandra*, *NuSTAR*'s background is spatially asymmetric across detectors, so we could not use a background region separate from our source region. Instead, we set the background exposure to

Table 4. Variability Analysis Data (3-8 keV)

Inst.	Proj. Code	Src. Counts (ph)	Bkg. Counts (ph)	Src. Exposure (10^6 cm 2 ·s)	Bkg. Exposure (10^6 cm 2 ·s)	ECF
<i>NuSTAR</i>	60101047002	978	426	21.6	-	0.734
	60701064002	1412	304	35.5	-	0.745
	60701064004	396	89	11.0	-	0.736
	60701064006	1497	333	40.3	-	0.746
<i>Chandra</i>	346	203	81	6.16	6.08	0.930
	3090	281	56	7.82	8.11	0.956
	4369	318	63	8.66	8.97	0.950
	11586	106	42	2.86	2.88	0.884
	12039	197	115	5.11	5.17	0.936
	12040	150	86	3.63	3.68	0.911
	14221	324	107	4.19	4.18	0.953
	15580	390	134	2.31	2.37	0.932
	14222	327	103	10.6	9.47	0.953
	14223	115	30	8.61	9.02	0.948
	16478	183	71	5.71	4.88	0.965
	17574	128	63	4.19	3.55	0.942

be the same as our source exposure, and used `nuskybgd` produced background maps to extract the background counts within our source region.

In general for both *NuSTAR* and *Chandra* the PSF (and therefore, the ECF) changes depending on the distance from the source to the optical axis. We use our extracted regions to measure the mean ECF for each observation. For *Chandra*, we generated simulated PSFs using the CIAO tool `simulate_psf` and MARX v5.4.0 and calculated the percentage of photons enclosed within the source region. For *NuSTAR*, we used *NuSTARDAS* product files to map the path of the optical axis for each observation and took the median x- and y-coordinate of its path. We then simulated the *NuSTAR* PSF based on the distance between the source and the optical axis and used this to calculate the ECF as was done for the *Chandra* observations.

2.7. Image deconvolution with LIRA

To detect the inner jet or any features in the western hotspot, for example the “bar” seen in *Chandra* images, possibly buried in the raw *NuSTAR* observations, we deconvolved the merged sky image of Pictor A (see Figure 1) with an effective point spread function (PSF).

We use a statistical tool called Low Count Image Reconstruction and Analysis (LIRA, Esch et al. 2004; Stein et al. 2015) to deconvolve images. Although LIRA was originally designed to detect the statistical significance of structures in low-count high-energy observations, it also has been used to deconvolve sky images (e.g., Kashyap et al. 2017; Reddy et al. 2021; Reddy et al. 2023). We refer the reader to Stein et al. (2015) for a full statistical treatment. Briefly, LIRA models the brightness distribution of an observation using two model images. One is a baseline with known sources of emission (e.g., core and background), which is specified by the user, and an added model, which is to be inferred containing any emission over the baseline, required to explain the observation. We can reconstruct the observation by convolving their sum with the PSF. LIRA performs Bayesian analysis using a flexible multi-scale representation of the observation to infer the posterior distribution of the added model and samples it with a Markov Chain Monte Carlo (MCMC) sampler to generate a series of images. These images represent the observation’s brightness distribution after subtracting the baseline. With `nuskybgd`-generated background as the baseline, we generate 2000 images after discarding the first 1000 images as *burn-in* and average them to produce a deconvolved image.

Due to the spatial dependence of *NuSTAR*’s PSF, using a single PSF to deconvolve both the core and the hotspot, which are separated by $\sim 4'$, may lead to artifacts in the output images. Hence, we separately deconvolve the core and the hotspot regions. Furthermore, to determine the energy dependence of the structure in the jet and the hotspot, we divide the image into two energy ranges of 3-12 keV and 12-78 keV, as shown in the top and bottom rows of Figure

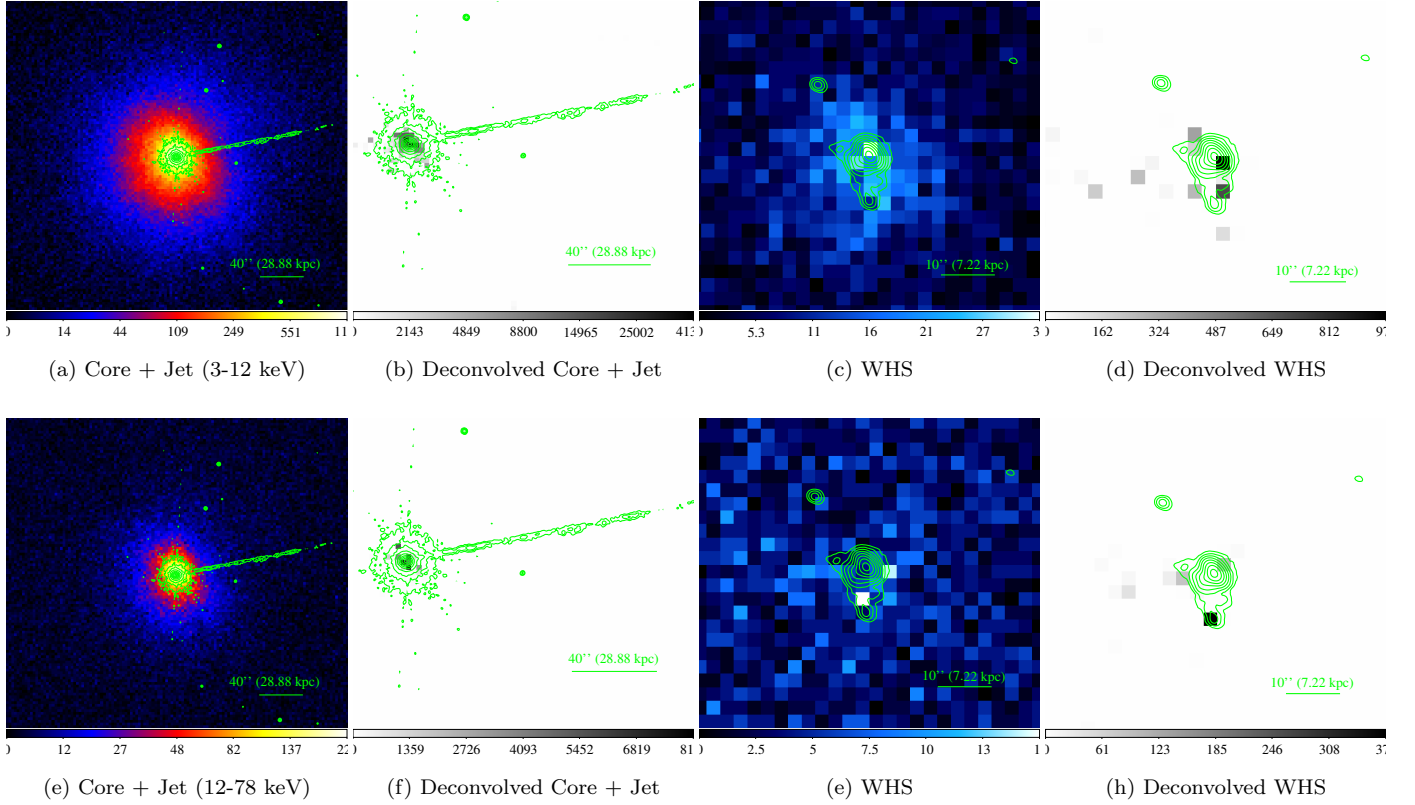


Figure 4. LIRA-deconvolved images of Pictor A with the *Chandra* contours overlaid on the top. (a) shows the deconvolved image of the core region where no evidence for an inner jet is found indicating its emission is within the error limits of the PSF of the core and background. (b) shows the deconvolved image of the western hotspot. The observed structure is roughly consistent with the *Chandra* observations.

4. The left and right two panels in each row show core and WHS images, respectively. We set the core image size to 128x128 and WHS to 64x64, following the input requirements of LIRA.

The top and bottom rows of panels in Figure 4 show the sky and LIRA-deconvolved images of the core and the WHS in the energy ranges 3-12 keV and 12-78 keV, respectively. We find no evidence for an inner jet in the core’s deconvolution in both the energy ranges (panels b and f), indicating its emission is within the error limits of the core’s PSF and background. This absence of emission is expected in the sense that the flux from the inner jet is close to the detection limit of NuSTAR. The 0.5-7 keV energy flux of the brightest feature in the inner jet is $\approx 2.5 \times 10^{-14}$ erg $\text{cm}^{-2} \text{s}^{-1}$, while the 3σ -sensitivity of NuSTAR with a 1 Ms exposure³ (about three times larger than our combined 300 ks exposure) is 2×10^{-15} erg $\text{cm}^{-2} \text{s}^{-1}$ (Harrison et al. 2013). Finally, because we also find no evidence for a jet beyond 12 keV (Fig. 4(e)), we use the estimated 10-30 keV sensitivity of 10^{-14} erg $\text{cm}^{-2} \text{s}^{-1}$ as an upper limit for each knot. Hence, we take 4×10^{-14} erg $\text{cm}^{-2} \text{s}^{-1}$ as an upper limit on the inner jet’s 10-30 keV flux.

Panels (d) and (f) show the LIRA-deconvolved images of the WHS in the 3-12 keV and 12-78 keV bands, respectively, where the detected structure appears spatially correlated with previously known features. The 3-12 keV images show point sources at the southern end of the bar and the hotspot, consistent with the structure found in *Chandra* images. Interestingly, the 12-78 keV band lacks a point source near the hotspot, but we find a bright point feature spatially coincident with the bar’s southern peak. This feature indicates the jet presumably produces an electron population capable of generating hard X-rays when it enters the turbulent hotspot region. However, the limited statistics in the bar region preclude a detailed spectral analysis and require a much deeper observation to understand the true nature of this hard X-ray emission.

³ Measured in the 6-10 keV band

3. RESULTS

We present the fit results for our analyses in Tables 5 (*NuSTAR* epochs 1, 2, and all epochs combined) and 6 (*Chandra* all epochs combined and *NuSTAR+Chandra* combined fit). The results for the individual *Chandra* epochs are given in Appendix Table A1. In these tables we give the best-fit values and 1σ posterior distribution of the model parameters detailed in Table 2 for each data set as calculated through our BXA analysis. We report only on the most likely models for a given epoch or combined fit as determined by the Bayesian evidence (see below). In all but one case, the powerlaw (PL), broken powerlaw (Bkn. PL), and double broken powerlaw (Dbl. Bkn. PL) were the three preferred models according to this metric (refer to Table 2 for exact definitions of these models). We report energy parameters ($E_{brk}, E_{brk,1}, E_{brk,2}$) in units of keV, normalizations (N_1) in units of nJy, and photon indices ($\Gamma, \Gamma_1, \Gamma_2, \Gamma_3$).

We compared the alternative models based on three different metrics which are suitable for comparing non-nested models. The first is the Bayesian evidence, defined as the integral over the parameter space: $Z = \int \pi(\vec{\theta}) \exp[-\frac{1}{2}C(\vec{\theta})] d\vec{\theta}$, where $\vec{\theta}$ is the parameter vector. The second is the Bayesian information criterion, $BIC = C - n \times \ln(d)$ (Schwarz 1978), where C is the log-likelihood value, d is the number of data points, and n is the number of degrees of freedom. The BIC is an approximation under the assumption that the posterior distribution is strongly single-peaked, which is well-supported by the posterior distributions for our data. The final comparison statistic we use is the Akaike information criterion, $AIC = C - 2 \times n$ (Akaike 1974). The AIC is a more conservative metric which measures the information loss of a specific model and is useful for determining if a model has the appropriate number of degrees of freedom. In all cases included in this study, comparing models using ΔAIC and ΔBIC only reinforces the paradigm established by the Bayesian evidence. As such, we omit these values from Tables 5 and 6. Although we emphasize that it is not useful for comparison nor is it used in fitting at any point, we do calculate the $\chi_{red}^2 = \chi^2/\text{DOF}$ for each model as a check of the goodness-of-fit. This value is calculated by loading the best-fit model from the BXA analysis into XSPEC and binning the spectra to at least 30 counts per bin using `ftgrouppha`. The Bayesian evidence, the relative probabilities of the different models (which are calculated directly from the Bayesian evidence), and the χ_{red}^2 are all recorded in Tables 5 and 6.

3.1. NuSTAR spectral fitting

According to the Bayesian evidence resulting from our analysis of the combined *NuSTAR* data (recorded in Table 5), the simple power-law is the slightly preferred model for the 3-20 keV band. (The broken power law and double broken power law appear at first to be acceptable, if slightly less-preferred models, but see discussion of parameter values below.) The exponential cutoff powerlaw, log-parabola, and thermal models are effectively ruled out by the evidence. The simple power law model is also favored when comparing the ΔAIC and ΔBIC for the different models.

The best-fit folded power law model and posterior range are plotted alongside the *NuSTAR* FPMA and FPMB data in the top panel of Figure 5, and the residuals of the model are plotted in the bottom panel. This simple power law fit of the 3-20 keV spectrum has a best-fit photon index of $\Gamma = 2.03 \pm 0.04$ and a normalization of $118.9_{-9.2}^{+8.7}$ nJy at 1 keV. The maximum likelihood value for the constant offset factor we introduce to account for sensitivity differences between the FPMA and FPMB modules is $f = 1.01 \pm 0.03$ which is in agreement with previous estimates of a $\pm 5\%$ calibration difference between the two detectors (Madsen et al. 2015).

We find no evidence of a spectral break or cutoff in our *NuSTAR* X-ray data alone. The maximum likelihood parameter values for the broken powerlaw and double broken powerlaw models are both asymptotic approximations of the simple power law. That is, the posterior distribution of the broken powerlaw is strongly peaked at a parameter distribution such that $\Gamma_1 \sim \Gamma_2$ and the posterior distribution of the double broken powerlaw is strongly peaked such that $\Gamma_1 \sim \Gamma_2 \sim \Gamma_3$.

We also fit the 2 epochs of *NuSTAR* data separately. The Bayesian evidence of the second epoch (which has triple the exposure of the first) again favored the simple powerlaw model, with the best-fit broken powerlaw and double broken powerlaw models being slightly less probable and showing little change in spectral index across the energy band. For the first epoch, the double broken powerlaw is actually the slightly preferred model, however the parameter best-fit values and errors make it clear that it is effectively equivalent to a single constant power-law spectrum, with $\Gamma_1 = 2.01_{-0.16}^{+0.15}$, $\Gamma_2 = 1.94_{-0.13}^{+0.17}$, and $\Gamma_3 = 1.96_{-0.14}^{+0.18}$.

Assuming a simple powerlaw as the correct model, the photon index showed no significant variation between the two major epochs, ranging from $\Gamma = 1.94_{-0.09}^{+0.10}$ for epoch 1 to $\Gamma = 2.05_{-0.04}^{+0.05}$ for epoch 2. However, the best-fit normalization changed substantially between the two epochs, with an approximately $\sim 50\%$ increase in value from epoch 1 to epoch 2, suggesting variability in the hard X-ray flux. This is further examined and quantified in Section 3.5.

Table 5. *NuSTAR* X-ray Spectral Fitting Results

NS-1	Powerlaw (PL)	$N_1 = 84.6^{+19.2}_{-12.4}$	$\Gamma = 1.94^{+0.10}_{-0.09}$	-	-	-0.12	0.271	37.8/49 = 0.771
	Broken powerlaw (Bkn. PL)	$N_1 = 92.9^{+22.2}_{-17.5}$	$\Gamma_1 = 2.00^{+0.16}_{-0.15}$	$E_{brk} = 4.03^{+0.65}_{-0.71}$	$\Gamma_2 = 1.93^{+0.12}_{-0.11}$	-0.07	0.304	37.0/47 = 0.796
	Double broken powerlaw* (Dbl. Bkn. PL*)	$N_1 = 93.9^{+21.1}_{-18.2}$	$\Gamma_1 = 2.01^{+0.15}_{-0.16}$	$\Gamma_2 = 1.94^{+0.17}_{-0.13}$	$E_{brk,1} = 3.98^{+0.72}_{-0.65}$	$\Gamma_3 = 1.96^{+0.18}_{-0.14}$	0.00	0.357
NS-2	PL*	$N_1 = 126.9^{+12.7}_{-9.9}$	$\Gamma = 2.05^{+0.05}_{-0.04}$	-	-	0.00	0.338	142.9/159 = 0.899
	Bkn. PL	$N_1 = 127.2^{+22.2}_{-21.8}$	$\Gamma_1 = 2.06^{+0.11}_{-0.13}$	$E_{brk} = 5.40^{+1.79}_{-1.65}$	$\Gamma_2 = 2.05^{+0.07}_{-0.07}$	-0.03	0.315	141.6/157 = 0.902
	Dbl. Bkn. PL	$N_1 = 125.8^{+24.7}_{-25.4}$	$\Gamma_1 = 2.05^{+0.14}_{-0.18}$	$\Gamma_2 = 2.05^{+0.10}_{-0.10}$	$E_{brk,1} = 4.03^{+0.68}_{-0.66}$	$\Gamma_3 = 2.04^{+0.09}_{-0.10}$	-0.01	0.330
NS-All	PL*	$N_1 = 118.9^{+8.7}_{-9.2}$	$\Gamma = 2.03^{+0.04}_{-0.04}$	-	-	0.00	0.373	196.9/211 = 0.933
	Bkn. PL	$N_1 = 120.4^{+24.0}_{-26.0}$	$\Gamma_1 = 2.04^{+0.14}_{-0.19}$	$E_{brk} = 3.97^{+0.72}_{-0.71}$	$\Gamma_2 = 2.02^{+0.05}_{-0.05}$	-0.08	0.310	196.0/209 = 0.938
	Dbl. Bkn. PL	$N_1 = 119.1^{+25.2}_{-24.0}$	$\Gamma_1 = 2.04^{+0.14}_{-0.17}$	$\Gamma_2 = 2.02^{+0.10}_{-0.10}$	$E_{brk,1} = 4.05^{+0.65}_{-0.73}$	$\Gamma_3 = 2.03^{+0.09}_{-0.09}$	-0.08	0.310

NOTE—* denotes the preferred model, according to the Bayesian evidence

NOTE—Break energies (E_{brk} , $E_{brk,1}$, $E_{brk,2}$) are reported in units of keV; 1 keV flux normalizations (N_1 – k_{ev}) are reported in units of nJy; photon indices (Γ , Γ_1 , Γ_2 , Γ_3) are dimensionless

NOTE—Refer to Table 2 for exact definitions of the models and their respective parameters.

Table 6. *Chandra* and *Chandra*+*NuSTAR* X-ray Spectral Fitting Results

Inst.-Epoch	Model	N_1 -keV (nJy)	param. 1	param. 2	param. 3 (keV)	param. 5	log(Z)	p(M-D)	χ^2 /dof
CH-All	PL	$N_1 = 95.1^{+0.7}_{-0.8}$	$\Gamma = 1.98^{+0.01}_{-0.01}$	-	-	-	-0.66	0.113	464.0/598 = 0.776
	Bkn. PL	$N_1 = 95.0^{+0.7}_{-0.7}$	$\Gamma_1 = 1.96^{+0.02}_{-0.02}$	$E_{brk} = 2.98^{+0.70}_{-0.51}$	$\Gamma_2 = 2.15^{+0.10}_{-0.09}$	-	-0.14	0.372	462.6/596 = 0.776
	DbI. Bkn. PL*	$N_1 = 95.0^{+0.7}_{-0.7}$	$\Gamma_1 = 1.95^{+0.02}_{-0.02}$	$\Gamma_2 = 2.20^{+0.16}_{-0.14}$	$E_{brk,1} = 3.04^{+0.42}_{-0.51}$	$\Gamma_3 = 1.92^{+0.23}_{-0.22}$	0.00	0.515	453.9/594 = 0.764
CH+NU-All	PL	$N_1 = 120.1^{+3.5}_{-3.8}$	$\Gamma = 2.01^{+0.01}_{-0.01}$	-	-	-	-3.36	4.36×10^{-4}	660.9/802 = 0.824
	Bkn. PL	$N_1 = 119.9^{+4.0}_{-4.2}$	$\Gamma_1 = 2.01^{+0.01}_{-0.01}$	$E_{brk} = 13.65^{+4.36}_{-9.26}$	$\Gamma_2 = 2.00^{+0.15}_{-0.19}$	-	-3.38	4.16×10^{-4}	462.6/596 = 0.776
	DbI. Bkn. PL*	$N_1 = 97.8^{+5.0}_{-4.4}$	$\Gamma_1 = 2.49^{+0.01}_{-0.11}$	$\Gamma_2 = 1.98^{+0.02}_{-0.03}$	$E_{brk,1} = 0.69^{+0.04}_{-0.03}$	$\Gamma_3 = 2.05^{+0.09}_{-0.18}$	0.00	0.999	453.9/594 = 0.764
	PL+Exp. Cutoff	$N_1 = 105.4^{+9.7}_{-9.5}$	$\Gamma = 1.90^{+0.05}_{-0.06}$	-	$E_{cut} = 57.53^{+14.6}_{-16.8}$	-	-	-	-

NOTE—* denotes the preferred model, according to the Bayesian evidence

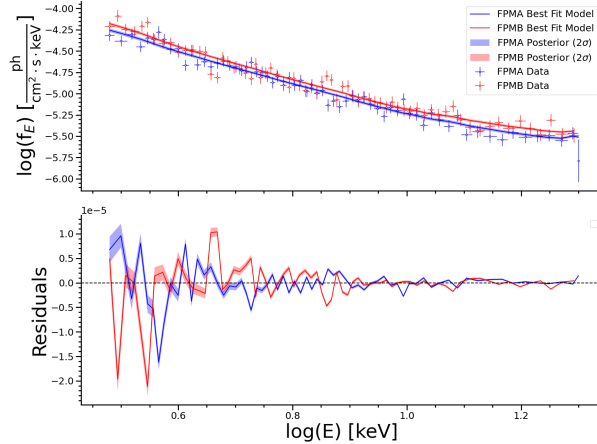


Figure 5. (Top) Photon flux density versus energy for the combined NuSTAR epochs, shown separately for the FPMA (blue) and FPMB (red) modules. For plotting purposes only, the data are collected into 66 and 69 spectral bins for the FPMA and FPMB detectors respectively across an energy range of 3-20 keV. Each point is the averaged photon flux as calculated using the source counts and exposure for that spectral bin. The solid line plots the flux density of the folded best-fit powerlaw model including the effects of galactic absorption. The shaded contours around either line displays the 2σ range in flux density of the posterior distribution. (Bottom) The residuals of the best-fit power law model and posterior distribution as compared to the spectral data. As with the top plot, the solid lines plots the residuals between the best-fit model and the data and the shaded contours plot the 2σ range of the posterior distribution for both the FPMA and FPMB modules.

3.2. Chandra X-ray spectrum

According to the Bayesian evidence resulting from our analysis of the combined *Chandra* data (recorded in Table 6), the double broken power-law is the slightly preferred model for the 0.5-7 keV band (although see discussion below). The broken power law and simple power law are also acceptable if slightly less-preferred models, while the exponential cutoff powerlaw, log-parabola, and thermal models are effectively ruled out by the evidence.

Interestingly, when we fit the individual epochs of *Chandra* data separately, the simple powerlaw (1, 3-5) and broken powerlaw (2, 6, 7) are consistently favored over the double broken powerlaw (albeit only slightly). The preference for the double broken powerlaw in the combined fit might be the result of variations from epoch to epoch which manifest as an additional spectral break in the combined data set. Because of this, and the weak constraints on the second break energy and third photon index, we instead opt to consider the broken power law model as the “true” spectral model as it is only slightly less preferred than the double broken powerlaw in the combined dataset.

The best-fit broken powerlaw model has a primary photon index of $\Gamma_1 = 1.95 \pm 0.02$, a secondary photon index of $\Gamma_2 = 2.15^{+0.10}_{-0.09}$, a break energy at $E_{brk} = 2.98^{+0.70}_{-0.51}$, and a normalization of $N_1 = 95.0 \pm 0.7$ nJy at 1 keV. This folded model and its posterior range are plotted alongside the combined 0.5-7 keV *Chandra* data in the top panel of Figure 6, and the residuals of the model are plotted in the bottom panel. These results are in rough agreement with [Hardcastle et al. \(2016\)](#), whose analysis of the *Chandra* observations of the Western hotspot also slightly preferred the broken power law model fit to the spectrum. The location of the break energy at just below the *NuSTAR* band combined with the preferred simple powerlaw model for the hard X-ray spectrum of the hotspot also provides more evidence in support of a singly broken powerlaw.

Similar to our *NuSTAR* analysis, comparing the changes in the best-fit single powerlaw models between various *Chandra* epochs reveals that the photon index varies little, ranging from $\Gamma = 1.93^{+0.06}_{-0.06}$ to $\Gamma = 2.01^{+0.04}_{-0.03}$. Also similarly, albeit smaller in scale, we see a roughly 10% decrease in the normalization from *Chandra* epoch 4 to epoch 5, or a 2.33σ change. This is similar to the variability previously reported by [Hardcastle et al. \(2016\)](#). The values of the normalization and integrated flux in the 3-8 keV flux band shared by both *NuSTAR* and *Chandra* across the different epochs of data from both telescopes are plotted in Figure 7, with the photon index in the lower panel. Further quantification and discussion of the X-ray variability is continued in Section 3.5.

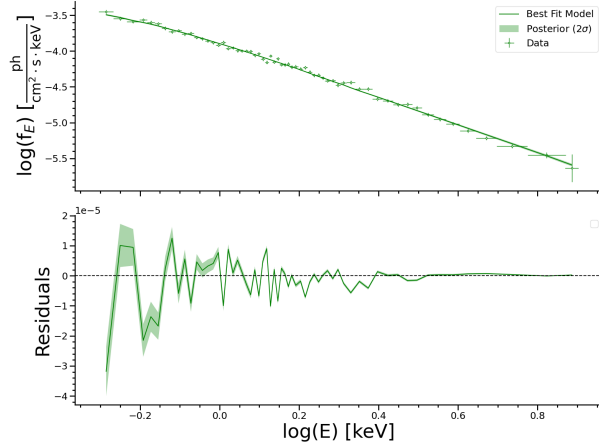


Figure 6. (Top) Photon flux versus energy for the combined *Chandra* data. For plotting purposes only, the data are collected into 187 spectral bins across an energy range of 0.5-7 keV. Each point is the averaged spectrum across the 11 observations for that spectral bin, calculated using the total counts and exposure for that spectral bin. The solid green line plots the flux of the best-fit broken power law model including the effects of galactic absorption. For visual purposes only, the background spectrum is subtracted. The shaded green contours around either line displays the 2σ range in flux density of the posterior distribution. (Bottom) The residuals of the best-fit power law model and posterior distribution as compared to the spectral data. As with the top plot, the solid green line plots the residuals between the best-fit model and the data and the shaded green contours plot the 2σ range of the posterior distribution.

3.3. Combined *Chandra* + *NuSTAR* X-ray spectrum

According to the Bayesian evidence resulting from our analysis of the combined fit of our *Chandra*+*NuSTAR* data (recorded in Table 6), the double broken powerlaw is the preferred model for the 0.5-20 keV wide band. However, similar to our analysis of the two telescopes independently, a close inspection of the parameter values reveals that this preference does not manifest as a “true” spectral break. The double broken powerlaw has an exceptionally steep primary photon index which is not seen in previous analyses ($\Gamma_1 = 2.49^{+0.01}_{-0.11}$) and a low energy for the primary spectral break ($E_{brk,1} = 0.69^{+0.04}_{-0.03}$). This is likely a case of overfitting and attempting to correct for offsets between the different datasets. The broken power law and simple power law are also acceptable if less-preferred models, while the exponential cutoff powerlaw, log-parabola, and thermal models are effectively ruled out by the evidence.

The best-fit broken power law model and posterior range are plotted alongside the combined *Chandra* and *NuSTAR* data in the top panel of Figure 8, and the residuals of the model are plotted in the bottom panel. This broken power law model has a best-fit photon indices of $\Gamma_1 = 2.25^{+0.01}_{-0.03}$ and $\Gamma_2 = 1.98^{+0.01}_{-0.01}$, a break energy of $E_{brk} = 0.76^{+0.07}_{-0.06}$ keV, and a normalization of $107.6^{+4.4}_{-3.8}$ nJy at 1 keV.

To constrain the possibility of a cutoff to the spectrum (which is of interest for its physical implications for the maximum electron energy, E_{max} ; see Section 4) we fit the broadband X-ray spectrum (3-78 keV) using a powerlaw with exponential cutoff, finding a 1σ lower limit of $E_{cut} > 40.7$ keV for the cutoff energy. The best-fit parameter values for the overall fit are included in Table 6, but since this model incorporates data for the entire *NuSTAR* spectrum, we do not attempt to compare to the other models via information criterion or the Bayesian evidence. (The same model fit to the 3-20 keV data range was significantly disfavored compared to the other models.

Although the Bayesian evidence suggests that the broken powerlaw and double broken powerlaw models are significantly more probable than the simple powerlaw model, a closer examination of the results suggest they must be interpreted with caution. Firstly, the best fit primary break energy value for both the broken and double broken powerlaw models is approximately ~ 0.75 keV, close to the lower boundary of the spectral range and differing from the value of ~ 3 keV for the *Chandra* fit alone. The photon index after the break is approximately ~ 2 , which is in agreement with the best fit simple powerlaw photon index calculated for most epochs of both *NuSTAR* and *Chandra* data. In the case of the double broken powerlaw model, the second spectral break shows no significant change in spectral index for before and after the second break (1.98 ± 0.02 to 2.03 ± 0.06), and thus can be disregarded. Importantly,

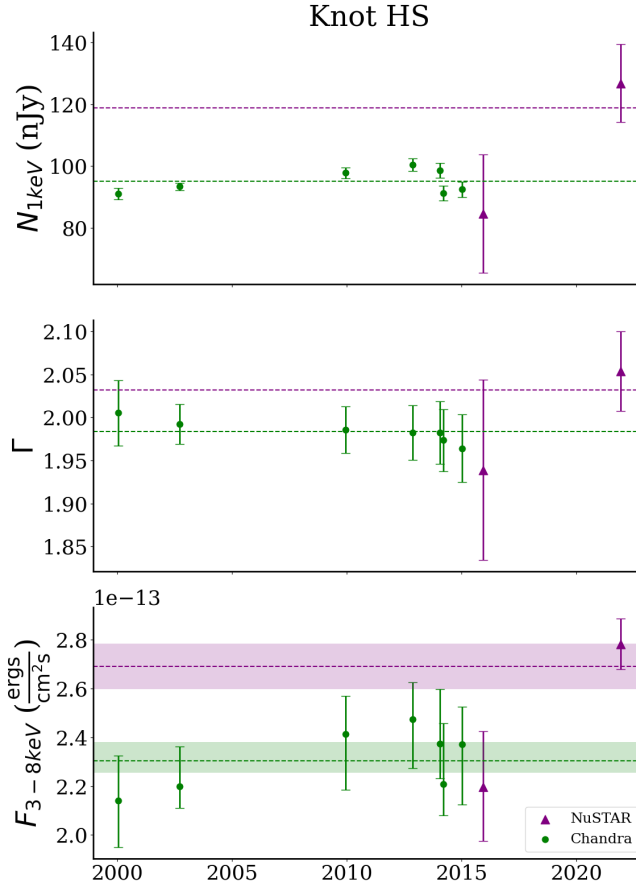


Figure 7. A plot showing the evolution of the powerlaw photon normalization at 1 keV, N_1 (top), the powerlaw spectral index, Γ (middle), and the integrated flux in the shared 3-8 keV band (bottom) over time. The error bars for the first two are determined via the Bayesian analysis, while the errors for the bottom plot are calculated via the `XSPEC` `cflux` command. The best-fit values for the combined data of all epochs for textitNuSTAR FPMA (red) and FPMB (blue) and *Chandra* (green) are plotted as dashed lines. The normalization shows slight changes over time with a significant offset between best-fit values between *NuSTAR* and *Chandra*. Despite large changes in the normalization between *NuSTAR* epochs 1 and 2, the uncertainties due to lower exposure limit the statistical significance of our variability analysis. In contrast, Γ shows little change over time and little variation between the different telescopes, maintaining a nearly constant spectrum ($\Gamma \sim 2$) across all data.

the joint fit also includes a relative normalization factor for *NuSTAR* to force agreement with *Chandra*; the value is $f \sim 0.80 \pm 0.02$, a larger difference than expected for instrumental effects alone. The combination of evident variability (which also complicated results of the *Chandra* analysis presented in the last section)

3.4. Spectral energy distribution

For comparison and to produce the most complete spectrum of Pictor A’s western hotspot to date, we collected multifrequency archival data from previous studies, including radio and infrared observational data from the VLA (Meisenheimer et al. 1997), observations from Spitzer (Werner et al. 2012), WISE (Isobe et al. 2017), and SPIRE (Isobe et al. 2020), as well as additional archival data recorded in the aforementioned studies.

The full spectral energy distribution (SED) of the western hotspot is shown in Figure 9. We include the model of Isobe et al. (2020) to describe the low energy emission, consisting of a primary cutoff powerlaw and an ‘excess’ broken cutoff powerlaw to account for the observed flux at mid- and far-infrared frequencies. We additionally plot νF_{ν} as calculated from the unfolded data of our independent *Chandra* and *NuSTAR* datasets. The data points are corrected for background, instrument response, and absorption using `XSPEC`’s `plot_ufspec` command.

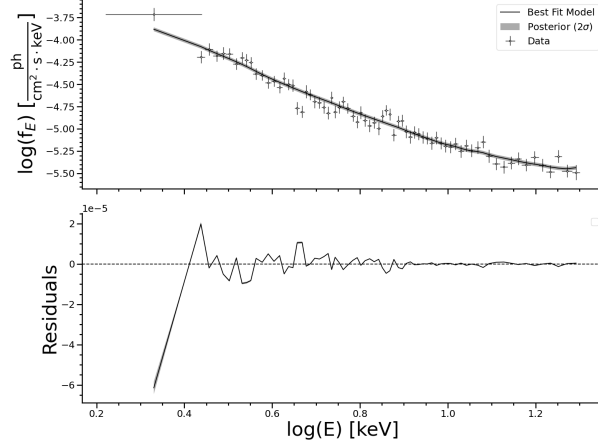


Figure 8. (Top) The combined spectral data of all 11 *Chandra* and 8 *NuSTAR* FPMA and FPMB observations used in this study fit by a single model. The data are binned into 70 spectral bins across an energy range of 0.5–20 keV for visual purposes only. The solid black line plots the flux of the best-fit broken power law model including the effects of galactic absorption and the contributions of background radiation. The shaded contours around the line displays the 2σ range in flux density of the posterior distribution. (Bottom) The residuals of the best-fit power law model and posterior distribution as compared to the spectral data. As with the top plot, the solid black line plots the best-fit residuals and the shaded contours plot the 2σ range of the posterior distribution.

There is an offset in normalization between our *NuSTAR* and *Chandra* data which is evident both in the SED and in the best-fit parameter values recorded in Table 6, suggesting that the hotspot may have been in a somewhat higher state during the recent *NuSTAR* observation. Because the XSPEC model by default normalizes the flux at 1 keV (technically below the *NuSTAR* sensitivity range), this apparent variability likely explains the apparent shift of the spectral break energy in the combined fit as an artifact of the forced agreement. A visual inspection of the SED suggests that there is indeed a slight break at around 2 keV. At higher energies, the spectral fits for essentially all data sets here considered agree on a very nearly perfectly constant spectrum with no other break or cutoff.

3.5. Variability analysis

We find strong evidence of statistically significant variability in the total *Chandra*-measured X-ray flux for the western hotspot. When we include all 11 *Chandra* observations, the returned p -value is $p = 2 \times 10^{-11}$, allowing us to reject the steady rate hypothesis at a significance of 6.76σ , approximately twice the significance over previous reports. We also analyzed smaller subsets of observations, in order to constrain the shortest timescale of the flux variability. For example, applying our variability analysis to only epochs 5 and 6 of the *Chandra* data, which are separated in time by approximately 2 months, still gives a p -value of $p = 9 \times 10^{-4}$, or 3.32σ . This suggests significant X-ray flux variations on the timescales of months, which by light-crossing time arguments would place an upper limit of $r < .01$ pc on the varying region. This result also supports the findings of [Hardcastle et al. \(2016\)](#), who reported a change in the flux of the western hotspot of approximately 10% on a timescale of approximately ~ 1 month.

For the variability analysis of the *NuSTAR* data alone, we recorded the necessary data outlined in Section 2.6 separately for both the FPMA and FPMB detectors. We then generated a combined data set, using the total photon counts, total exposure, and average ECF from the two detectors, which are presented in Table 3. We then analyzed this combined data set using our maximum likelihood analysis, which returns $p = 0.082$, equivalent to 1.74σ .

The two epochs of *NuSTAR* data alone do not demonstrate highly significant variability, but when we include the full 22 year time-span of *NuSTAR* and *Chandra* in the shared 3–8 keV energy band (data recorded in 4), our maximum likelihood method returned a p -value below the machine precision value of R , $p < 2.2 \times 10^{-16}$, giving a significance of at least $\sigma > 8.21$. This result for the Western hotspot is the strongest evidence yet of short-timescale (\sim years) variability across the X-ray hotspot population. These results, along with additional tests for short-term variability are summarized in Table 7, where we list the instrument(s), epochs, resulting p -values and equivalent significance, and the longest time baseline of the data set.

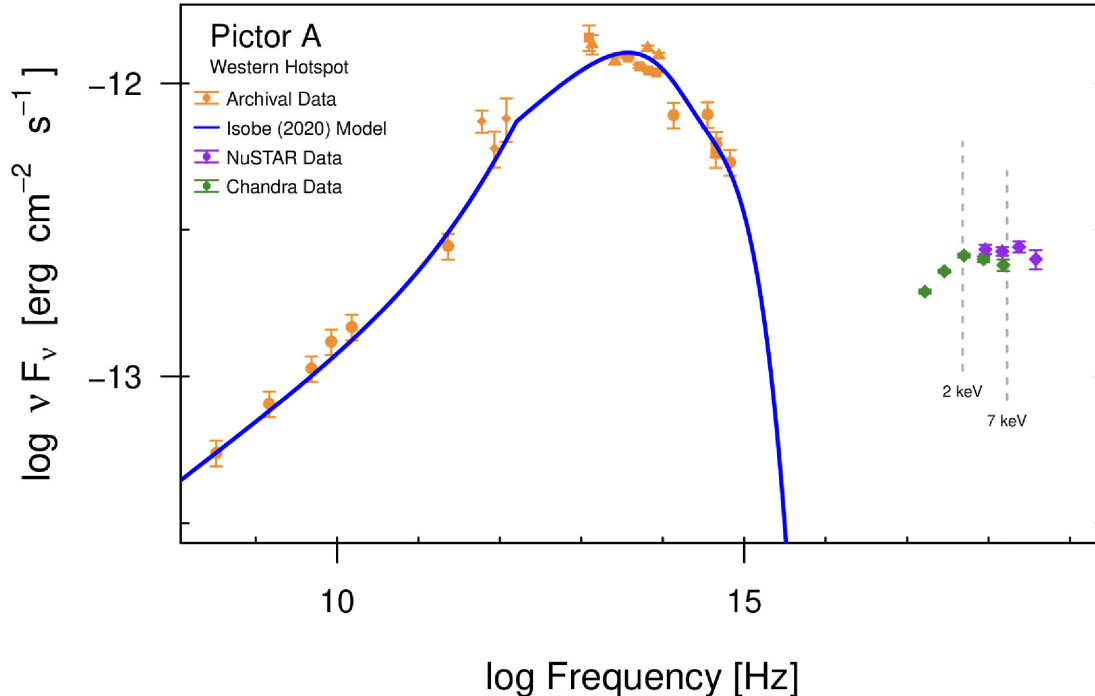


Figure 9. The SED of the Western hotspot of Pictor A. Archival data taken from Meisenheimer et al. (1997) (circles), Werner et al. (2012) (squares), Isobe et al. (2017) (triangles), and Isobe et al. (2020) (diamonds) are plotted in orange. This archival data is consistent with a synchrotron spectrum modeled as a cutoff powerlaw and a broken cutoff powerlaw to account for excess IR emission, thought to be due to synchrotron emission from discrete zones with enhanced magnetic field strength (Isobe et al. 2020). We plot the unfolded X-ray spectral data points based on the best-fit models for *NuSTAR* (purple) and *Chandra* (green). We calculated the unfolded data points corrected for the instrument response and the galactic absorption using XSPEC’s `plot_ufspec` command, which scales the data by a factor equal to the ratio of the unfolded model flux and the folded model flux. The model predictions from the two observatories shows a significant difference in the measured flux, which is further evidence of short timescale variability.

Table 7. Variability results

Instrument	Epochs	p -value	Significance (σ)	(Δt)
<i>Chandra</i>	1-3	0.064	1.85	9 yr
<i>Chandra</i>	5-6	8.68e-4	3.13	3 mo
<i>Chandra</i>	4-7	3.19e-5	3.75	2 yr
<i>Chandra</i>	All	3.33e-11	6.53	15 yr
<i>NuSTAR</i>	2	0.820	0.23	1 wk
<i>NuSTAR</i>	All	0.082	1.74	6 yr
<i>NuSTAR+Chandra</i>	All	<2.2e-16	>8.21	22 yr

4. DISCUSSION

The origins of the X-ray emission in AGN hotspots has been discussed extensively in the literature (e.g., Tavecchio et al. 2000; Celotti et al. 2001; Hardcastle et al. 2004; Georganopoulos et al. 2006; Mingo et al. 2017; Migliori et al. 2020). Initial studies of Pictor A in particular suggested that a standard one-zone SSC model was incapable of explaining the broadband SED, including an unusually high X-ray-to-radio flux ratio (Wilson et al. 2001), as well as X-ray jet/counter-jet ratio and X-ray variability (Hardcastle et al. 2016). Although already disfavored, we can test the IC-CMB hypothesis by comparing the extended X-ray spectrum with that in the radio, since if IC-CMB is

responsible for the anomalous X-ray emission we expect to find that the X-ray spectral index is roughly equivalent to the low-frequency (\sim MHz) radio spectral index (Georganopoulos et al. 2006; Jester et al. 2006). The X-ray spectrum is not subject to the same requirements under a synchrotron origin, since the electrons producing the X-rays are distinct from those producing the radio emission. In agreement with previous work (e.g. Hardcastle et al. 2016; Thimmappa et al. 2020) our results strongly disfavor an inverse Compton origin for the X-rays of the western Pictor A hotspot, based on the variability as well as the mismatch between the X-ray and radio spectral indices ($\Gamma_X = 2.03 \pm .03$ vs. $\Gamma_R = 1.74 \pm .02$ respectively).

The minimum-energy (equipartition) magnetic field strength has been estimated at 0.36 mG (Isobe et al. (2017), though later work has argued for a value 3-10 times larger under the hypothesis of highly magnetized substructures of scale less than a 100 pc (Isobe et al. 2020). Under a synchrotron scenario the observed lower bound on the spectral cutoff energy of 41 keV corresponds to electron Lorentz factors $\gamma \sim 1 - 3 \times 10^6$ using these values. The corresponding synchrotron cooling timescale $\tau_{syn} \sim (16/\gamma)(B/1\text{ G})^{-2}$ yr using these values is 1-5 days. Since the cooling timescale is proportional to the square root of the corresponding photon energy, this 3-4 times shorter than that expected in the *Chandra* band. In any case, these timescales are shorter than the minimum variability timescales observed with *Chandra*, and correspond to very small spatial scales, possibly as small as light-days. In contrast the observed variability on month-year timescales implies \sim pc spatial scales of is in keeping with the observations of Tingay et al. (2008), who studied the Pictor A western hotspot using the Very Long Baseline Array (VLBA), finding multiple resolved pc-scale radio components within the hotspot. They suggested the X-rays could be produced by discrete substructures within the hotspot which are highly magnetized, which also could explain the observed excess emission in the IR (Isobe et al. 2017, 2020).

The lack of high spatial resolution in the X-rays prevents us from spatially resolving the variability, but clearly the total flux we observe is integrated over many discrete regions, and therefore the low level (tens of percent) variability we see in aggregate translates to much larger-amplitude flaring within the actual small-scale region undergoing variability. Future coordinated monitoring campaigns with e.g., the VLBA and a next-generation sensitive and high-spatial-resolution X-ray telescope such as *AXIS* may reveal these sites and the particle acceleration within them in action.

5. CONCLUSIONS

We have presented the results of a comprehensive analysis of the Western hotspot of Pictor A using a recent deep *NuSTAR* observation combined with archival data from both *NuSTAR* and *Chandra*. We presented separate (soft/hard) and combined fits to the wide X-ray band (0.5-20 keV) and analyzed the X-ray emission for variability using the maximum likelihood method of Meyer et al. (2023). The main results of these analyses are:

(i) We found that the *NuSTAR* data alone is best fit by a simple power law of photon index $\Gamma = 2.03 \pm 0.04$ and a normalization at 1 keV of $N_1 = 118.9_{-9.2}^{+8.7}$. We do not find any evidence for a spectral break or cutoff energy in the hard X-ray band. The difference in normalization between the recent 2021 observations and previous epochs of both *Chandra* and *NuSTAR* data suggests variability within the western hotspot.

(ii) We found that the *Chandra* data alone is best fit by a broken power law of photon indices $\Gamma_1 = 1.95 \pm 0.02$ and $\Gamma_2 = 2.15_{-0.09}^{+0.10}$, a break energy at $E_{brk} = 2.98_{-0.51}^{+0.70}$, and a normalization of $N_1 = 95.0 \pm 0.7$ nJy at 1 keV.

(iii) We found that the combined *Chandra* and *NuSTAR* data are best fit by a broken power law model, with a best-fit photon indices of $\Gamma_1 = 2.25_{-0.03}^{+0.01}$ and $\Gamma_2 = 1.98_{-0.01}^{+0.01}$, a break energy of $E_{brk} = 0.76_{-0.06}^{+0.07}$ keV, and a normalization of $107.6_{-3.8}^{+4.4}$ nJy at 1 keV. However, the fit requires a significant offset factor of $f = 0.80$ for *NuSTAR* relative to *Chandra*. This suggests that the hotspot flux may have been higher during the recent *NuSTAR* epoch and that interpretations of the joint fit must be made cautiously.

(iv) The maximum likelihood variability analysis of the *Chandra* observations of the western hotspot finds statistically significant (6.5σ) variations in the 0.4-8 keV X-ray emission, confirming the results of Hardcastle et al. (2016) and Thimmappa et al. (2020). We also confirm a significant (3.3σ) variation on a timescale of ~ 2 months, placing an upper limit on the size of the varying region of $r < .01$ pc.

(v) The variability analysis of the *NuSTAR* data alone is unable to find evidence of statistically significant variability in the hard, 3-20 keV X-ray flux, with a maximum significance of 1.74σ . However, analyzing both the *NuSTAR* and *Chandra* data in the shared 3-8 keV energy range gives the most significant detection of variability yet, at $> 8.2\sigma$.

Collectively, these results suggest a synchrotron origin for the hotspot X-ray emission, as the alternative beamed IC-CMB model is incapable of explaining either the rapid X-ray variability or the discrepancy between the measured X-ray spectral index ($\Gamma_X = 2.03 \pm 0.03$) and the expected low-frequency radio spectral index ($\Gamma_R = 1.74 \pm 0.02$).

The emerging picture of the hotspot is of multiple localized, highly magnetized, pc-scale substructures emitting X-ray predominantly via synchrotron radiation in agreement with previous research (e.g., Tingay et al. 2008; Isobe et al. 2020). This paradigm is capable of explaining the rapid X-ray variability and the difference in spectral index between the radio and X-rays. Magnetic reconnection models are a possible explanation for *in situ* acceleration in smaller regions and can produce electrons at the required TeV energies (e.g. Werner et al. 2016; Bodo et al. 2021).

Follow-up observations of Pictor A with *NuSTAR* might allow for a more significant detection of variability in the hard X-ray band and could confirm the flaring detected in the recent observations. The next major evolution will be the study of other nearby hotspots in the hard X-ray band. As mentioned previously, this is not a feasible task for *NuSTAR* due to its angular resolution and the lower X-ray flux of most other hotspots relative to Pictor A’s western hotspot. Next generation X-ray missions with higher angular resolution and sensitivity such as *FORCE* (Nakazawa et al. 2018), *HXMT* (Zhang et al. 2020), and *Athena* (Barret et al. 2023) should be capable of analyzing whether Pictor A’s western hotspot is an outlier or a typical representative of the X-ray jet population.

1 This research has made use of data from the *NuSTAR* mission led by the California Institute of Technology and
 2 managed by NASA’s Jet Propulsion Laboratory, as well as software provided by the High Energy Astrophysics Science
 3 Archive Research Center (HEASARC), a service of the Astrophysics Science Division at NASA/GSFC and the High
 4 Energy Astrophysics Division of the Smithsonian Astrophysical Observatory. The observations were supported by the
 5 *NuSTAR* Guest Observer program. This research also made use of XSPEC (Arnaud 1996) and BXA (Buchner et al.
 6 2014).

7 This paper employs a list of Chandra datasets, obtained by the Chandra X-ray Observatory, contained in the
 8 Chandra Data Collection (CDC) 243 doi:10.25574/cdc.243. This research also made use of software provided by the
 9 Chandra X-ray Center (CXC) in the application packages CIAO (Fruscione et al. 2006), ChIPS (Germain et al. 2006),
 10 and Sherpa (Freeman et al. 2001; Doe et al. 2007; Burke et al. 2020).

REFERENCES

- Akaike, H. 1974, IEEE Transactions on Automatic Control, 19, 716
- Andrae, R., Schulze-Hartung, T., & Melchior, P. 2010, arXiv e-prints, arXiv:1012.3754. <https://arxiv.org/abs/1012.3754>
- Arnaud, K. A. 1996, in Astronomical Society of the Pacific Conference Series, Vol. 101, Astronomical Data Analysis Software and Systems V, ed. G. H. Jacoby & J. Barnes, 17
- Arshakian, T. G., & Longair, M. S. 2000, MNRAS, 311, 846, doi: 10.1046/j.1365-8711.2000.03098.x
- Barret, D., Albouys, V., Herder, J.-W. d., et al. 2023, Experimental Astronomy, 55, 373, doi: 10.1007/s10686-022-09880-7
- Blandford, R. D., & Königl, A. 1979, ApJ, 232, 34, doi: 10.1086/157262
- Bodo, G., Tavecchio, F., & Sironi, L. 2021, MNRAS, 501, 2836, doi: 10.1093/mnras/staa3620
- Breiding, P., Meyer, E. T., Georganopoulos, M., et al. 2017, ApJ, 849, 95, doi: 10.3847/1538-4357/aa907a
- . 2023, MNRAS, 518, 3222, doi: 10.1093/mnras/stac3081
- Buchner, J. 2016, BXA: Bayesian X-ray Analysis, Astrophysics Source Code Library, record ascl:1610.011. <http://ascl.net/1610.011>
- . 2021, The Journal of Open Source Software, 6, 3001, doi: 10.21105/joss.03001
- Buchner, J., Georgakakis, A., Nandra, K., et al. 2014, A&A, 564, A125, doi: 10.1051/0004-6361/201322971
- Burke, D., Laurino, O., Wmclaugh, et al. 2020, sherpa/sherpa: Sherpa 4.12.1, 4.12.1, Zenodo, doi: 10.5281/zenodo.3944985
- Cash, W. 1979, ApJ, 228, 939, doi: 10.1086/156922
- Celotti, A., Ghisellini, G., & Chiaberge, M. 2001, MNRAS, 321, L1, doi: 10.1046/j.1365-8711.2001.04160.x
- Chartas, G., Worrall, D. M., Birkinshaw, M., et al. 2000, ApJ, 542, 655, doi: 10.1086/317049
- Churazov, E., Sunyaev, R., Revnivtsev, M., et al. 2007, A&A, 467, 529, doi: 10.1051/0004-6361:20066230
- Dabhade, P., Mahato, M., Bagchi, J., et al. 2020, A&A, 642, A153, doi: 10.1051/0004-6361/202038344
- Doe, S., Nguyen, D., Stawarz, C., et al. 2007, in Astronomical Society of the Pacific Conference Series, Vol. 376, Astronomical Data Analysis Software and Systems XVI, ed. R. A. Shaw, F. Hill, & D. J. Bell, 543
- Erlund, M. C., Fabian, A. C., Blundell, K. M., Moss, C., & Ballantyne, D. R. 2007, MNRAS, 379, 498, doi: 10.1111/j.1365-2966.2007.11962.x

- Esch, D. N., Connors, A., Karovska, M., & van Dyk, D. A. 2004, *The Astrophysical Journal*, 610, 1213
- Fabian, A. C. 2012, *ARA&A*, 50, 455, doi: [10.1146/annurev-astro-081811-125521](https://doi.org/10.1146/annurev-astro-081811-125521)
- Fanaroff, B. L., & Riley, J. M. 1974, *MNRAS*, 167, 31P, doi: [10.1093/mnras/167.1.31P](https://doi.org/10.1093/mnras/167.1.31P)
- Freeman, P., Doe, S., & Siemiginowska, A. 2001, in *Society of Photo-Optical Instrumentation Engineers (SPIE) Conference Series*, Vol. 4477, *Astronomical Data Analysis*, ed. J.-L. Starck & F. D. Murtagh, 76–87, doi: [10.1117/12.447161](https://doi.org/10.1117/12.447161)
- Fruscione, A., McDowell, J. C., Allen, G. E., et al. 2006, in *Society of Photo-Optical Instrumentation Engineers (SPIE) Conference Series*, Vol. 6270, *Society of Photo-Optical Instrumentation Engineers (SPIE) Conference Series*, ed. D. R. Silva & R. E. Doxsey, 62701V, doi: [10.1117/12.671760](https://doi.org/10.1117/12.671760)
- Garmire, G. P., Bautz, M. W., Ford, P. G., Nousek, J. A., & Ricker, George R., J. 2003, in *Society of Photo-Optical Instrumentation Engineers (SPIE) Conference Series*, Vol. 4851, *X-Ray and Gamma-Ray Telescopes and Instruments for Astronomy.*, ed. J. E. Truemper & H. D. Tananbaum, 28–44, doi: [10.1117/12.461599](https://doi.org/10.1117/12.461599)
- Georganopoulos, M., & Kazanas, D. 2003, *ApJL*, 589, L5, doi: [10.1086/375796](https://doi.org/10.1086/375796)
- Georganopoulos, M., Perlman, E. S., Kazanas, D., & McEnery, J. 2006, *ApJL*, 653, L5, doi: [10.1086/510452](https://doi.org/10.1086/510452)
- Germain, G., Milaszewski, R., McLaughlin, W., et al. 2006, in *Astronomical Society of the Pacific Conference Series*, Vol. 351, *Astronomical Data Analysis Software and Systems XV*, ed. C. Gabriel, C. Arviset, D. Ponz, & S. Enrique, 57
- Gordon, C., & Arnaud, K. 2021, *PyXspec: Python interface to XSPEC spectral-fitting program*, *Astrophysics Source Code Library*, record ascl:2101.014. <http://ascl.net/2101.014>
- Gruber, D. E., Matteson, J. L., Peterson, L. E., & Jung, G. V. 1999, *ApJ*, 520, 124, doi: [10.1086/307450](https://doi.org/10.1086/307450)
- Hardcastle, M. J., Birkinshaw, M., Cameron, R. A., et al. 2002, *ApJ*, 581, 948, doi: [10.1086/344409](https://doi.org/10.1086/344409)
- Hardcastle, M. J., & Croston, J. H. 2005, *MNRAS*, 363, 649, doi: [10.1111/j.1365-2966.2005.09469.x](https://doi.org/10.1111/j.1365-2966.2005.09469.x)
- Hardcastle, M. J., Harris, D. E., Worrall, D. M., & Birkinshaw, M. 2004, *ApJ*, 612, 729, doi: [10.1086/422808](https://doi.org/10.1086/422808)
- Hardcastle, M. J., Lenc, E., Birkinshaw, M., et al. 2016, *MNRAS*, 455, 3526, doi: [10.1093/mnras/stv2553](https://doi.org/10.1093/mnras/stv2553)
- Harris, D. E., Biretta, J. A., Junor, W., et al. 2003, *ApJL*, 586, L41, doi: [10.1086/374773](https://doi.org/10.1086/374773)
- Harris, D. E., Carilli, C. L., & Perley, R. A. 1994, *Nature*, 367, 713, doi: [10.1038/367713a0](https://doi.org/10.1038/367713a0)
- Harris, D. E., & Krawczynski, H. 2006, *ARA&A*, 44, 463, doi: [10.1146/annurev.astro.44.051905.092446](https://doi.org/10.1146/annurev.astro.44.051905.092446)
- Harris, D. E., & Krawczynski, H. 2007, in *Revista Mexicana de Astronomia y Astrofisica Conference Series*, Vol. 27, *Revista Mexicana de Astronomia y Astrofisica*, vol. 27, 188, doi: [10.48550/arXiv.astro-ph/0604527](https://doi.org/10.48550/arXiv.astro-ph/0604527)
- Harris, D. E., Massaro, F., & Cheung, C. C. 2010, in *American Institute of Physics Conference Series*, Vol. 1248, *X-ray Astronomy 2009; Present Status, Multi-Wavelength Approach and Future Perspectives*, ed. A. Comastri, L. Angelini, & M. Cappi, 355–358, doi: [10.1063/1.3475257](https://doi.org/10.1063/1.3475257)
- Harrison, F. A., Craig, W. W., Christensen, F. E., et al. 2013, *ApJ*, 770, 103, doi: [10.1088/0004-637X/770/2/103](https://doi.org/10.1088/0004-637X/770/2/103)
- Harrison, F. A., Craig, W. W., Christensen, F. E., et al. 2013, *The Astrophysical Journal*, 770, 103, doi: [10.1088/0004-637x/770/2/103](https://doi.org/10.1088/0004-637x/770/2/103)
- HI4PI Collaboration, Ben Bekhti, N., Flöer, L., et al. 2016, *A&A*, 594, A116, doi: [10.1051/0004-6361/201629178](https://doi.org/10.1051/0004-6361/201629178)
- Isobe, N., Koyama, S., Kino, M., et al. 2017, *ApJ*, 850, 193, doi: [10.3847/1538-4357/aa94c9](https://doi.org/10.3847/1538-4357/aa94c9)
- Isobe, N., Sunada, Y., Kino, M., et al. 2020, *ApJ*, 899, 17, doi: [10.3847/1538-4357/ab9d1c](https://doi.org/10.3847/1538-4357/ab9d1c)
- Jester, S., Harris, D. E., Marshall, H. L., & Meisenheimer, K. 2006, *ApJ*, 648, 900, doi: [10.1086/505962](https://doi.org/10.1086/505962)
- Kashyap, V. L., van Dyk, D. A., McKeough, K., et al. 2017, *Proceedings of the International Astronomical Union*, 12, 284
- Knuth, K. H., Habeck, M., Malakar, N. K., Mubeen, A. M., & Placek, B. 2014, *arXiv e-prints*, arXiv:1411.3013. <https://arxiv.org/abs/1411.3013>
- Kraft, R. P., Forman, W. R., Jones, C., et al. 2002, *ApJ*, 569, 54, doi: [10.1086/339062](https://doi.org/10.1086/339062)
- Madsen, K. K., Beardmore, A. P., Forster, K., et al. 2017, *AJ*, 153, 2, doi: [10.3847/1538-3881/153/1/2](https://doi.org/10.3847/1538-3881/153/1/2)
- Madsen, K. K., Harrison, F. A., An, H., et al. 2014, in *Society of Photo-Optical Instrumentation Engineers (SPIE) Conference Series*, Vol. 9144, *Space Telescopes and Instrumentation 2014: Ultraviolet to Gamma Ray*, ed. T. Takahashi, J.-W. A. den Herder, & M. Bautz, 91441P, doi: [10.1117/12.2056643](https://doi.org/10.1117/12.2056643)
- Madsen, K. K., Harrison, F. A., Markwardt, C. B., et al. 2015, *ApJS*, 220, 8, doi: [10.1088/0067-0049/220/1/8](https://doi.org/10.1088/0067-0049/220/1/8)
- Marshall, H. L., Hardcastle, M. J., Birkinshaw, M., et al. 2010, *ApJL*, 714, L213, doi: [10.1088/2041-8205/714/2/L213](https://doi.org/10.1088/2041-8205/714/2/L213)
- McNamara, B. R., Kazemzadeh, F., Rafferty, D. A., et al. 2009, *ApJ*, 698, 594, doi: [10.1088/0004-637X/698/1/594](https://doi.org/10.1088/0004-637X/698/1/594)
- Meisenheimer, K., Yates, M. G., & Roeser, H. J. 1997, *A&A*, 325, 57

- Meyer, E. T., Sparks, W. B., Georganopoulos, M., et al. 2016, *ApJ*, 818, 195, doi: [10.3847/0004-637X/818/2/195](https://doi.org/10.3847/0004-637X/818/2/195)
- Meyer, E. T., Shaik, A., Tang, Y., et al. 2023, *Nature Astronomy*, doi: [10.1038/s41550-023-01983-1](https://doi.org/10.1038/s41550-023-01983-1)
- Migliori, G., Grandi, P., Palumbo, G. G. C., Brunetti, G., & Stanghellini, C. 2007, *ApJ*, 668, 203, doi: [10.1086/520870](https://doi.org/10.1086/520870)
- Migliori, G., Orienti, M., Coccato, L., et al. 2020, *MNRAS*, 495, 1593, doi: [10.1093/mnras/staa1214](https://doi.org/10.1093/mnras/staa1214)
- Mingo, B., Hardcastle, M. J., Ineson, J., et al. 2017, *MNRAS*, 470, 2762, doi: [10.1093/mnras/stx1307](https://doi.org/10.1093/mnras/stx1307)
- Mullin, L. M., Riley, J. M., & Hardcastle, M. J. 2008, *MNRAS*, 390, 595, doi: [10.1111/j.1365-2966.2008.13534.x](https://doi.org/10.1111/j.1365-2966.2008.13534.x)
- Nakazawa, K., Mori, K., Tsuru, T. G., et al. 2018, in *Society of Photo-Optical Instrumentation Engineers (SPIE) Conference Series*, Vol. 10699, *Space Telescopes and Instrumentation 2018: Ultraviolet to Gamma Ray*, ed. J.-W. A. den Herder, S. Nikzad, & K. Nakazawa, 106992D, doi: [10.1117/12.2309344](https://doi.org/10.1117/12.2309344)
- Reddy, K., Georganopoulos, M., & Meyer, E. T. 2021, *ApJS*, 253, 37, doi: [10.3847/1538-4365/abd8d7](https://doi.org/10.3847/1538-4365/abd8d7)
- Reddy, K., Georganopoulos, M., Meyer, E. T., Keenan, M., & Kollmann, K. E. 2023, *The Astrophysical Journal Supplement Series*, 265, 8, doi: [10.3847/1538-4365/aca321](https://doi.org/10.3847/1538-4365/aca321)
- Revnivtsev, M., Gilfanov, M., Sunyaev, R., Jahoda, K., & Markwardt, C. 2003, *A&A*, 411, 329, doi: [10.1051/0004-6361:20031386](https://doi.org/10.1051/0004-6361:20031386)
- Sambruna, R. M., Gambill, J. K., Maraschi, L., et al. 2004, *ApJ*, 608, 698, doi: [10.1086/383124](https://doi.org/10.1086/383124)
- Sambruna, R. M., Maraschi, L., Tavecchio, F., et al. 2001, in *American Institute of Physics Conference Series*, Vol. 587, *Gamma 2001: Gamma-Ray Astrophysics*, ed. S. Ritz, N. Gehrels, & C. R. Shrader, 256–260, doi: [10.1063/1.1419409](https://doi.org/10.1063/1.1419409)
- Schwarz, G. 1978, *The Annals of Statistics*, 6, 461, doi: [10.1214/aos/1176344136](https://doi.org/10.1214/aos/1176344136)
- Smith, R. K., Brickhouse, N. S., Liedahl, D. A., & Raymond, J. C. 2001, *ApJL*, 556, L91, doi: [10.1086/322992](https://doi.org/10.1086/322992)
- Snios, B., Wykes, S., Nulsen, P. E. J., et al. 2019, *ApJ*, 871, 248, doi: [10.3847/1538-4357/aafaf3](https://doi.org/10.3847/1538-4357/aafaf3)
- Stein, N. M., van Dyk, D. A., Kashyap, V. L., & Siemiginowska, A. 2015, *The Astrophysical Journal*, 813, 66
- Sun, X.-N., Yang, R.-Z., Rieger, F. M., Liu, R.-Y., & Aharonian, F. 2018, *A&A*, 612, A106, doi: [10.1051/0004-6361/201731716](https://doi.org/10.1051/0004-6361/201731716)
- Sunada, Y., Morimoto, A., Tashiro, M. S., et al. 2022, *PASJ*, 74, 602, doi: [10.1093/pasj/psac022](https://doi.org/10.1093/pasj/psac022)
- Tavecchio, F., Maraschi, L., Sambruna, R. M., & Urry, C. M. 2000, *ApJL*, 544, L23, doi: [10.1086/317292](https://doi.org/10.1086/317292)
- Thimmappa, R., Stawarz, L., Marchenko, V., et al. 2020, *ApJ*, 903, 109, doi: [10.3847/1538-4357/abb605](https://doi.org/10.3847/1538-4357/abb605)
- Tingay, S. J., Lenc, E., Brunetti, G., & Bondi, M. 2008, *AJ*, 136, 2473, doi: [10.1088/0004-6256/136/6/2473](https://doi.org/10.1088/0004-6256/136/6/2473)
- Weisskopf, M. C., Tananbaum, H. D., Van Speybroeck, L. P., & O'Dell, S. L. 2000, in *Society of Photo-Optical Instrumentation Engineers (SPIE) Conference Series*, Vol. 4012, *X-Ray Optics, Instruments, and Missions III*, ed. J. E. Truemper & B. Aschenbach, 2–16, doi: [10.1117/12.391545](https://doi.org/10.1117/12.391545)
- Werner, G. R., Uzdensky, D. A., Cerutti, B., Nalewajko, K., & Begelman, M. C. 2016, *ApJL*, 816, L8, doi: [10.3847/2041-8205/816/1/L8](https://doi.org/10.3847/2041-8205/816/1/L8)
- Werner, M. W., Murphy, D. W., Livingston, J. H., et al. 2012, *ApJ*, 759, 86, doi: [10.1088/0004-637X/759/2/86](https://doi.org/10.1088/0004-637X/759/2/86)
- Wik, D. R., Hornstrup, A., Molendi, S., et al. 2014, *ApJ*, 792, 48, doi: [10.1088/0004-637X/792/1/48](https://doi.org/10.1088/0004-637X/792/1/48)
- Wilson, A. S., Young, A. J., & Shopbell, P. L. 2001, *ApJ*, 547, 740, doi: [10.1086/318412](https://doi.org/10.1086/318412)
- Worrall, D. M. 2009, *A&A Rv*, 17, 1, doi: [10.1007/s00159-008-0016-7](https://doi.org/10.1007/s00159-008-0016-7)
- Worrall, D. M., Birkinshaw, M., Young, A. J., et al. 2012, *MNRAS*, 424, 1346, doi: [10.1111/j.1365-2966.2012.21320.x](https://doi.org/10.1111/j.1365-2966.2012.21320.x)
- Zhang, S.-N., Li, T., Lu, F., et al. 2020, *Science China Physics, Mechanics, and Astronomy*, 63, 249502, doi: [10.1007/s11433-019-1432-6](https://doi.org/10.1007/s11433-019-1432-6)

APPENDIX

A. *NUSTAR* BACKGROUND MODELS

We briefly detail the various background components here; a more complete overview can be found in (Wik et al. 2014).

Internal background. This element models radiation resulting from the environment of *NuSTAR*'s orbit and consists of two major components. The first is a featureless continuum, modeled as a broken power law with a break at 124 keV which dominates the background above 30 keV. The second is a collection of fluorescence and activation lines which dominates from approximately 20-30 keV, with weaker lines present up to ~ 100 keV.

Aperture background. The *NuSTAR* optical and focal plane modules are separated by an unenclosed mast. As a result, far away, off-axis stray light can leak into the aperture stop and strike the detector. Some of this stray light is blocked by the optics bench, resulting in a variable, spatially non-uniform background gradient across the detectors. The cosmic X-ray background (CXB) is the main contributor to this 'aperture' background, which dominates the background spectrum below 20 keV. `nuskybgd` uses the canonical HEAO-1 A2 spectral model for the CXB (Gruber et al. 1999; Revnivtsev et al. 2003; Churazov et al. 2007).

Scattered background. The *NuSTAR* detectors are also affected by reflected and scattered X-rays from parts of the observatory. The main sources of these X-rays are the CXB, the Sun, and the Earth. These radiation sources are subdominant at all energies, but can contribute significantly at low energies. In particular, during periods of heightened solar activity, the solar background appears as a ~ 1 keV thermal spectrum which can rival the aperture background radiation flux in the 3-5 keV energy range.

fCXB. The 'focused' CXB (fCXB) is a background radiation component resulting from unresolved sources within the FOV. The contribution of the fCXB is subdominant at all energies, but can contribute significantly below 15 keV, with a magnitude of approximately 10% of the CXB flux.

The `nuskybgd` package uses `XSPEC`⁴ (Arnaud 1996) to fit the spectrum of the entire background across the *NuSTAR* detector modules, taking into account each component and any spatial variations present. `nuskybgd` groups the input spectrum to a minimum of 30 counts per bin and calculates the parameter normalizations using the χ^2 statistic. Within `XSPEC`, the background model is defined using a combination of four different models. `apbgd` and `fxapbgd` model the 'aperture' and 'focused aperture' or 'fCXB' components and are both defined as cutoff power-law components (`cutoffpl`) with a photon index of $\Gamma = 1.29$ and a high-energy cutoff of $E = 41.13$ keV. The `line_bgd` component models the fluorescence and activation line elements of the 'internal' background component and the Solar thermal emission of the 'scattered' background. It is comprised of 29 different Lorentzian (`lorentz`) line profiles and a thermal plasma component (`appec`) with temperature $kT = 1.15$. The final element is the `particle_bgd` component which models the featureless continuum of the 'internal' background as a broken power-law with photon indices of $\Gamma_1 = -0.05, \Gamma_2 = -0.85$ and a break energy of $E_{brk} = 124$ keV.

We defined the background using 3 concentric annular regions which excluded emission from Pictor A and its jet and hotspot. An image example of these annular background regions for one of our *NuSTAR* observations is shown in Figure A1. The spectral parameters of each model component such as the power-law photon indices and the line energies and widths are set by `nuskybgd` and fixed prior to fitting and do not change from observation to observation. Only the normalizations of these components are free to vary during the background fitting process. The normalizations of each component are recorded for each observation in Supplemental Table 1 in units of $\text{ph}\cdot\text{cm}^{-2}\cdot\text{s}^{-1}\cdot\text{keV}^{-1}$.

B. RESULTS FOR INDIVIDUAL *CHANDRA* EPOCHS

In the main manuscript we have reported the results of our analysis of the western hotspot spectrum using *NuSTAR* data alone in Table 5 and the analysis of the total *Chandra* and the combined *NuSTAR+Chandra* datasets in Table 6. Due to the number and length, the results for individual *Chandra* epochs are reported here in Appendix Table A1.

⁴ <https://heasarc.gsfc.nasa.gov/xanadu/xspec>

Table A1. Individual *Chandra* epoch X-ray Spectral Fitting Results

NOTE— * denotes the preferred model, according to the Bayesian evidence

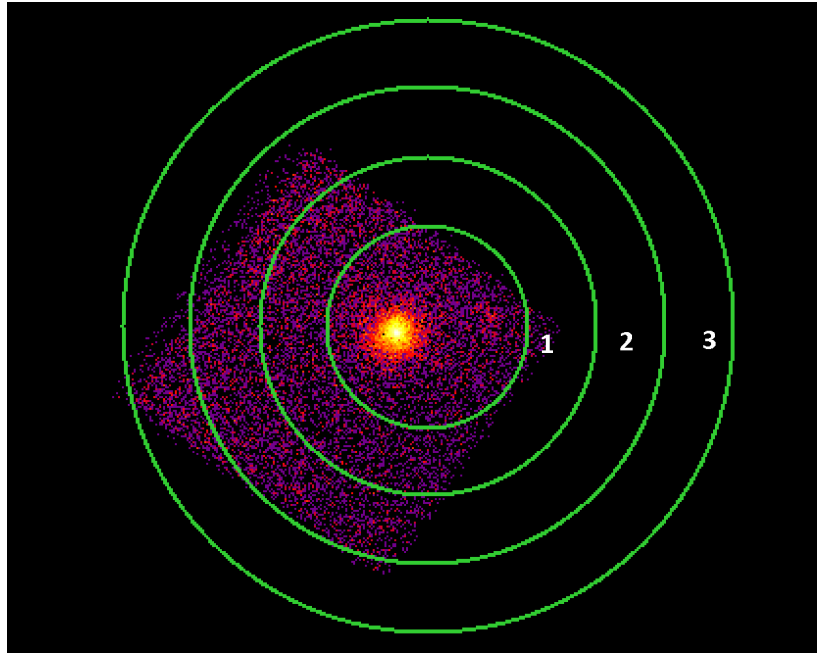


Figure A1. An image of source Pictor A and its western hotspot generated from *NuSTAR* epoch 1. The 3 green concentric circles define the annular background regions which are used by the `nuskybgd` package to map and calculate *NuSTAR*'s asymmetric background radiation. The first annulus is centered around the source and hotspot to exclude its source emission. The two outer annuli are defined such that their inner radii are equal to the outer radii of the preceding annulus to maximize coverage of the image. The region sections which include pixels outside the detector's FOV do not impact the spectral analysis as the exposure value is 0.